AD-A127 060 THE EFFECTS OF CORONA AND ANGLE OF ARRIVAL ON THE EMP 1/1
RESPONSE OF CABLES..(U) ELECTRO MAGNETIC APPLICATIONS
INC ALBUQUERQUE NM S R ROGERS ET AL. FEB 83
UNCLASSIFIED HDL-CR-83-004-1 DAAK21-80-C-0004 F/G 9/5 NL

END
DATE
FILMED
5 -83
DTIC

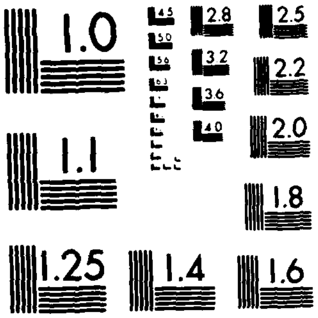

MICROCOPY RESOLUTION TEST CHART
NATIONAL BUREAU OF STANDARDS-1963-A

ADA 127 060

[illegible]

[illegible] on the [illegible] Response of Cables Lying on the Surface of the Earth

[illegible]

[illegible]

[illegible]

DTIC
ELECTE
APR 2 1 1983
S D
A

UNCLASSIFIED

SECURITY CLASSIFICATION OF THIS PAGE (When Data Entered)

REPORT DOCUMENTATION PAGE

READ INSTRUCTIONS
BEFORE COMPLETING FORM

1. REPORT NUMBER HDL-CR-83-004-1	2. GOVT ACCESSION NO. A127060	3. RECIPIENT'S CATALOG NUMBER

4. TITLE (and Subtitle)

The Effects of Corona and Angle of Arrival on the EMP Response of Cable Lying on the Surface of the Earth

5. TYPE OF REPORT & PERIOD COVERED

Contractor Report

6. PERFORMING ORG. REPORT NUMBER

7. AUTHOR(s)

S. R. Rogers
R. A. Perala

HDL Contact:
William Scharf

8. CONTRACT OR GRANT NUMBER(s)

DAAK21-80-C-0004

9. PERFORMING ORGANIZATION NAME AND ADDRESS

Electro Magnetic Applications, Inc.
1025 Hermosa Blvd., SE, P.O. Box 8482
Albuquerque, NM 87198

10. PROGRAM ELEMENT, PROJECT, TASK AREA & WORK UNIT NUMBERS

11. CONTROLLING OFFICE NAME AND ADDRESS

Harry Diamond Laboratories
2800 Powder Mill Road
Adelphi, MD 20783

12. REPORT DATE

February 1983

13. NUMBER OF PAGES

83

14. MONITORING AGENCY NAME & ADDRESS(if different from Controlling Office)

15. SECURITY CLASS. (of this report)

UNCLASSIFIED

15a. DECLASSIFICATION/DOWNGRADING SCHEDULE

16. DISTRIBUTION STATEMENT (of this Report)

Approved for public release; distribution unlimited.

17. DISTRIBUTION STATEMENT (of the abstract entered in Block 20, if different from Report)

18. SUPPLEMENTARY NOTES

HDL Project: E050E3
DRCMS Code: 36AA.6000.62704

19. KEY WORDS (Continue on reverse side if necessary and identify by block number)

EMP
cable coupling
corona

20. ABSTRACT (Continue on reverse side if necessary and identify by block number)

This report establishes that corona is not a significant factor in determining the coupling of source-region EMP to long cables positioned on or near the earth. A parametric comparison is given for the effect of angle of arrival on various lengths of cables exposed to source-region EMP. In addition, these calculations show that worst-case surface cable response is not necessarily caused by the largest peak amplitude incident field. Instead, the response tends to be more directly related to the time integral of the late time portions of the incident electric field.

DD FORM 1 JAN 73 1473 EDITION OF 1 NOV 65 IS OBSOLETE

UNCLASSIFIED

SECURITY CLASSIFICATION OF THIS PAGE (When Data Entered)

CONTENTS

FIGURES

FIGURES (Cont'd)

FIGURES (Cont'd)

TABLE

CHAPTER I

INTRODUCTION

Recently [1], the effects of soil and dielectric nonlinearities on the response of surface cables exposed to an electromagnetic pulse (EMP) from a nuclear burst were studied. In that study, it was found that voltage levels on the cable were large enough in many cases to cause air breakdown. However, air breakdown was not a feature incorporated into that surface cable model. Therefore, the intent of the present study is to incorporate air breakdown into that model. The objective is to determine the significance of air breakdown in determining surface cable response.

The total air breakdown process is complex and for this reason it is not fully understood. The air breakdown process can be divided into two phases, corona and arcing (or streamering). Corona is the first mechanism to occur in the air breakdown process, and is the only process examined in this study. The principal reason for concern over corona effects is that it is felt that the presence of a corona sheath around a conductor would tend to lower its characteristic impedance and thereby increase the conductor current.

Although the emphasis in this study is on the cable response in the source region environment, results are also calculated for cables in an ambient air environment in order to compare corona effects for both environments. In addition, a study is done to determine angle of arrival effects upon surface cables in the source region.

In Chapter II, the air breakdown model (corona) used in determining the air conductivity is discussed. In Chapter III the surface cable model is presented. The results of this study are presented in Chapter IV. Finally, conclusions from this investigation and recommendations for future work are given in Chapter V.

It was found in this study that corona does not appear to be a major factor which affects the response of surface cables. The presence of the nearby lossy earth damps out the corona effects. It was found, however, that the worst case surface cable response is not necessarily caused by the largest peak amplitude incident field. The lossy cable propagation constant damps out the high frequency response associated with the peak field, and the response tends to be more directly related to the time integral of the late time portions of the incident electric field.

CHAPTER II

CORONA MODEL

2.1 Definitions and Fundamental Concepts

The fundamental processes in corona and air breakdown involve collision ionization by free electrons. These electrons, when accelerated by an electric field, collide with air molecules, ionizing them and producing other free electrons and positive ions.

For the corona process to begin, therefore, free electrons, called triggering electrons, must exist. These free electrons can arise from any of several sources, such as thermal ionization, radiation, or photoionization. For the tactical nuclear environment, the triggering electrons are principally supplied by gamma ray photoionization from the nuclear detonation. In ambient air, such as would exist outside the nuclear source region, which is the case for high altitude EMP studies, the triggering electrons are provided by natural events such as cosmic rays. At sea level and standard temperature and pressure, this background source is reported to be on the order of 1×10^7 to 2×10^7 electron-ion pairs/(m^3-sec) [2,3]. It should be noted that in addition to this generation mechanism, free electrons are lost by recombination and attachment. These processes provide an ambient air conductivity of approximately 10^{-13} mho/m, which confirms the observation that ambient air is an excellent insulator.

In the presence of an impressed electric field, these triggering electrons are accelerated and travel by means of drift and diffusion. At low frequencies, drift is the primary mechanism, and at microwave frequencies, diffusion is most important [4]; therefore, for our purposes we will consider mainly electron drift.

As the electrons travel, they collide with molecules and produce other free electrons and positive ions, a process referred to as collision ionization. The resulting additional electrons plus the original are referred to as an electron avalanche.

Much of the literature on corona and air breakdown has to do with corona between two electrodes spaced rather closely together. This is different from our interest, which concerns a surface cable illumined by a large transient EMP from a distant source. Nonetheless, the essential physics of what happens in the air medium is the same. It should also be pointed out that corona processes are very complex, and are sensitive to electrode shapes and polarities, electrode impurities, surface contaminations, air pressure, impurities in the air, and humidity. Thus, there are many variables which play a role, and it is not within the scope of this report to consider all possible cases. The scope is, therefore, limited to the basic mechanisms and important effects on the surface cable response.

2.2 Corona Air Conductivity Formulation

The corona model used in this study considersthe effects of the avalanche rate G ($\sec^{-1}$), the electron attachment rate α_e ($\sec^{-1}$), electron-ion recombination β(m^3/sec), negative and positive ion recombination rate γ(m^3/sec), electron mobility μ_e ($m^2/V \cdot \sec$), and ion mobility μ_i ($m^2/V \cdot \sec$). G, α_e and μ_e are all functions of electric field E, relative air density ρ_r, and percent water vapor P (except for G). β depends upon P, and γ and μ_i depend upon ρ_r. Table 2.1 summarizes the formulas required to compute these coefficients. These are based on analytical fits to measured data, and their bases are discussed elsewhere [5] and will not be repeated here.

The continuity equation appropriate for consideration of electrons only can be stated

$$\frac{dn_e}{dt} + (\alpha_e - G)n_e = Q(t) \qquad (2.1)$$

where n_e is the number density of electrons (m^{-3}) and Q(t) is the ionizing source function which is the cosmic ray background radiation from high altitude EMP case and is the gamma ray photoionization rate for the source region case.

One can consider, in addition, the effects of the positive ion density n_+ and the negative ion density n_- and write the following coupled differential equations in a manner similar to equation 2.1:

TABLE 2.1 AIR CHEMISTRY COEFFICIENT FORMULAS. ALL UNITS ARE ESU [6]

Calculation of Erel:

$$\mathrm{Erel} = \frac{E}{\rho_r} / (1+2.457P^{0.834}) \quad \text{for } \frac{E}{\rho_r} < 0.07853(1+2.457P^{0.834})$$

$$\mathrm{Erel} = \frac{E}{\rho_r} - 1.195P^{0.834} \quad \text{for } \frac{E}{\rho_r} > 3.015+1.195P^{0.834}$$

$$\mathrm{Erel} = \left[\sqrt{\frac{E}{\rho_r} + \left(\frac{0.6884P^{0.834}}{2}\right)^2} - \frac{0.6884P^{0.834}}{2}\right]^2 \quad \text{for all other } \frac{E}{\rho_r}$$

Where P is the per cent water vapor and ρ_r is relative air density. Note: E is in esu, where Eesu = Emks/3x10^4

Calculation of Electron Attachment Rate α_e:

$$\alpha_e = \frac{100-P}{100} (\alpha_3(1+0.344P)+\alpha_2)$$

$$\alpha_2 = 1.22\times10^8 \rho_r e^{-21.15/\mathrm{Erel}}$$

$$\alpha_3 = \rho_r^2 (6.2\times10^7+8.\times10^{10}\mathrm{Erel}^2)/(1+10^3\mathrm{Erel}^2(\mathrm{Erel}(1+0.03\mathrm{Erel}^2))^{1/3})$$

Calculation of Electron Mobility, μ_e:

$$\mu_e = \frac{100\mu_a}{100-P+PXR}; \quad R = 1.55+210/(1+11.8\mathrm{Erel}+7.2\mathrm{Erel}^2)$$

$$\mu_a = 10^6(((16.8+\mathrm{Erel})/(0.63+26.7\mathrm{Erel}))^{0.6})/\rho_r$$

Calculation of Avalanche Rate, G:

$$G = 5.7\times10^8 \rho_r Y^5/(1+0.3Y^{2.5}); \quad Y = \frac{\mathrm{Erel}}{100}$$

Calculation of Ion Mobility, μ_i:

$$\mu_i = 750/\rho_r$$

Calculation of electron-ion recombination coefficient β, and ion-ion neutralization coefficient, γ:

$$\gamma = 2\times10^{-7} + \rho_r\, 2.1\times10^{-6}$$

$$\beta = 2\times10^{-7} + 2.8\times10^{-6} (P)^{1/3}$$

$$\left.\begin{aligned}
&\frac{dn_e(t)}{dt} + [\beta n_+(t) + \alpha_e - G]\, n_e\,(t) = Q(t),\\
&\frac{dn_-(t)}{dt} + [\gamma n_+(t)]\, n_-(t) = \alpha_e\, n_e(t),\\
&\frac{dn_+(t)}{dt} + [\beta n_e(t) + \gamma n_-(t)]\, n_+(t) = Q(t) + G\, n_e(t),\\
&n_+(t) = n_e(t) + n_-(t).
\end{aligned}\right\} \qquad (2.2)$$

In addition, one needs to solve for the air conductivity $\sigma(t)$ according to

$$\sigma(t) = q(\mu_e n_e + \mu_i(n_- + n_+)) \qquad (2.3)$$

where q is the fundamental electronic charge. It is clear that only three of equations 2.2 need to be solved, the other being redundant. It is interesting to solve these equations in the steady state ($\frac{d}{dt} = 0$) with the ambient $Q(\approx 10^7)$. If this is done, one obtains $n_e = .2/m^3$, and $n_+ \approx n_- = 7.3 \times 10^9/m^3$, and $\sigma = 2 \times 10^{-13}$ mho/m. Thus, there are very few free electrons in ambient air, and the ambient air conductivity is mainly caused by the presence of ions.

It is noted that this formulation does not include photoionization of the air caused by photons generated in the electron avalanche. The formulation then will not predict streamering or arcing. This is a deficiency in the model, because streamering and arcing have been observed on test objects in EMP simulators [7]. For all cases considered in this study, the relative air density is unity and the percent water vapor is zero.

The finite difference technique used in solving these equations at each time step and cable location warrants discussion. It was found that prohibitively small cable length and time increments were required for computational stability using conventional central differenced finite difference techniques. It was found that a more stable solution is obtained by using exponential differencing of the air conductivity equations. To implement this technique, it is noted that if s(t) is constant over the time interval Δt, then the differential equation

$$\frac{\partial f}{\partial t} + \alpha f = s(t) \tag{2.4}$$

has the solution

$$f(t+\Delta t) = f(t)e^{-\alpha\Delta t} + \left(\frac{1 - e^{-\alpha\Delta t}}{\alpha}\right) s(t+\Delta t/2) \tag{2.5}$$

compared to the central differenced form

$$f(t+\Delta t) = f(t)\,\frac{1 - \alpha\Delta t/2}{1 + \alpha\Delta t/2} + \frac{\Delta t}{1 + \alpha\Delta t/2}\quad(s(t+\Delta t/2)). \tag{2.6}$$

For small values of $\alpha\Delta t$, these solutions are equivalent, however, if sudden increases in α are expected, (2.5) is the more stable solution.

CHAPTER III

THE NONLINEAR SURFACE CABLE MODEL

3.1 Background

The model (SBLINE) which was previously used to study soil and dielectric breakdown effects on insulated surface cables is discussed in Reference 1. The details of that model will not be repeated here, but the model will be summarized to provide background information so that the modification of the model to include air breakdown can be understood.

The model for a spatial increment Δz is shown in Figure 3.1. The elements of this model are identified as follows:

$$G_{arc} = 4\sigma_s \, r_{arc} \tag{3.1}$$

is the ionized soil region conductance per unit length,

$$C_{arc} = 4\varepsilon_s \, r_{arc} \tag{3.2}$$

is the ionized soil region capacity per unit length,

$$r_{arc} = \sqrt{\frac{I}{4\sigma_s \, E_{SBR}}} \tag{3.3}$$

is the arc radius,

$$C_{surface} = \frac{1}{2}\left(C_s\left(1 + \frac{r_{arc}}{\Delta z/2}\right) + C_A\right), \tag{3.4}$$

$$C_s = \frac{2\pi\,\varepsilon_s}{\ell n\left({}^{a_3}\!/_{a_2}\right)} \tag{3.5}$$

is the soil capacity per unit length

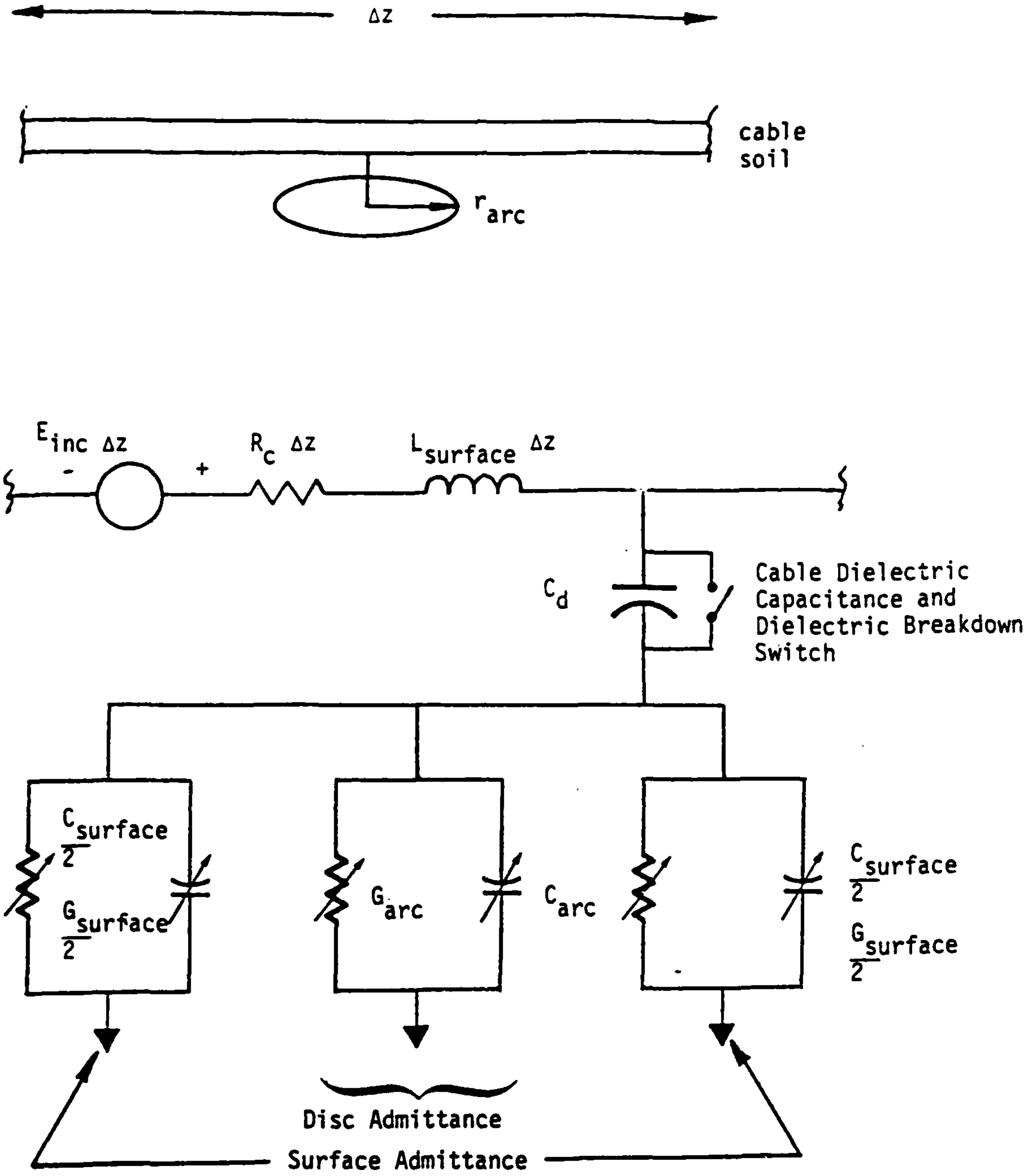

Figure 3.1 Surface Table Model Which Includes Soil and Dielectric Nonlinearities

$$G_{surface} = \frac{1}{2}\left(G_s\left(1 + \frac{r_{arc}}{\Delta z/2}\right) + G_A\right), \text{ and} \tag{3.6}$$

$$G_s = \frac{\sigma_s}{\varepsilon_s} C_s \tag{3.7}$$

is the soil conductance per unit length. The air medium parameters G_A and C_A can be obtained merely by replacing the subscript s by A and noting the impressed air conductivity $\sigma_A(t)$ is time varying. The surface cable inductance is given by,

$$L_{surface} = \frac{\mu_o}{\pi} \ln\left(a_{32} / a_1\right) \ln\left(a_{31} / a_1\right) \Big/ \left[\ln\left(a_{32} / a_1\right) + \ln\left(a_{31} \quad a\right)\right], \tag{3.8}$$

R_c is the DC resistance of the cable conductor,

a_1 is the radius of the cable conductor,

a_2 is the outer radius of the dielectric sheath,

E_{SBR} is the surface breakdown electric field for soil,

$$a_{3\,(1,2)} = .794\ \delta_{(s,A)} + a_2, \tag{3.9}$$

$$C_d = \frac{2\pi\ \varepsilon_d}{\ln\left(a_2/a_1\right)} \tag{3.10}$$

is the dielectric capacity per unit length,

$$\delta_{(s,A)} = \sqrt{\frac{t}{2\pi\ \mu_0\ \sigma_{(s,A)}}} \tag{3.11}$$

is the skin depth of the soil (s) or air (A) and it is computed from the time after an excitation arrives at the location of interest, and E^{inc} is the incident electric field.

The time domain equivalent of the telegraphers' equations for the three node equation model is:

$$\left.\begin{aligned}
\frac{\partial(V_d+V_s)}{\partial z} &= -L\,\frac{\partial I}{\partial t} - R_c I + E^{inc}\,(z,t)\\
\frac{\partial I}{\partial z} &= -C_d\,\frac{\partial V_d}{\partial t} - G_d V_d\\
\frac{\partial I}{\partial z} &= -C_t\,\frac{\partial V_s}{\partial t} - G_t V_s,
\end{aligned}\right\} \qquad (3.12)$$

where V_d is the voltage across the dielectric, V_s is the soil (or air) voltage, I is the cable current,

$$C_t = C_{surface} + C_{arc}, \qquad (3.13)$$

$$G_t = G_{surface} + G_{arc}, \qquad (3.14)$$

and all other parameters are defined in equations 3.1 through 3.11.

3.2 Incorporation of Corona in the Transmission Line Formulatic

3.2.1 Background

In order to extend the SBLINE code to include air breakdown, it is necessary to use a two conductor transmission line equivalent in which one conductor is the cable and the other conductor represents the corona sheath. This modification enables the corona sheath, when formed, to conduct current and partially shield the cable conductor. In addition, the time varying admittance and impedance requires use of time varying components in the telegraphers' equations for conductor i (i = 1,2):

$$\left.\begin{aligned}
\frac{\partial I_i}{\partial z} &= \sum_{j=1}^{2}\left[-\frac{\partial}{\partial t}\left(C_{ij}V_j\right) - G_{ij}V_j\right] + I_i^{sc}\\
\text{and}\quad \frac{\partial V_i}{\partial z} &= \sum_{j=1}^{2}\left[-\frac{\partial}{\partial t}\left(L_{ij}I_j\right) - R_{ij}I_j\right] + E_i^{inc},
\end{aligned}\right\} \qquad (3.15)$$

where V_i is the voltage drop from the $i^{\underline{th}}$ conductor to ground, I_i is the current on the $i^{\underline{th}}$ conductor, C_{ij} is the capacitance per unit length matrix element, G_{ij} is the conductance per unit length matrix element, L_{ij} is the inductance per unit length matrix element, R_{ij} is the resistance per unit length matrix element, I_i^{sc} is the impressed current density (zero here) on the $i^{\underline{th}}$ conductor, and E_i^{inc} is the incident electric field on the $i^{\underline{th}}$ conductor (see Figure 3.2).

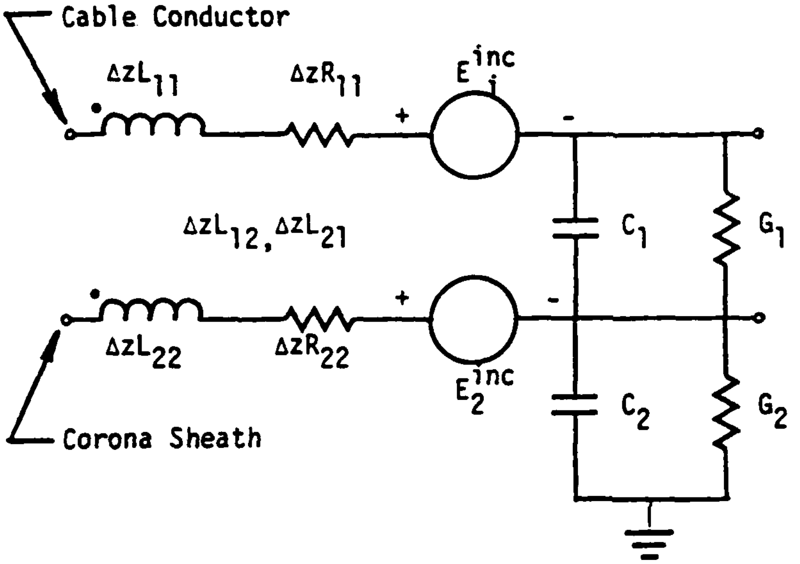

$$\Delta z[G_{ij}] = \begin{pmatrix} G_1 & -G_1 \\ -G_1 & G_1 + G_2 \end{pmatrix}$$

$$\Delta z[C_{ij}] = \begin{pmatrix} C_1 & -C_1 \\ -C_1 & C_1 + C_2 \end{pmatrix}$$

Figure 3.2 Two Conductor Three Node Transmission Line Equivalent

This transmission line equivalent is used for modelling the surface cable including air, soil, and dielectric nonlinearities. Description of the elements of these models are given in the next two subparagraphs.

3.2.2 Wire Over a Perfect Ground Plane

The significance of air breakdown on cable response is most easily demonstrated when air is the only medium surrounding the cable. For an insulated cable elevated a height h above a perfect ground, the equivalent transmission line model is shown in Figure 3.3. The circuit elements of this model are also defined explicitly in that figure.

The air circumscribing the cable after breakdown is assumed to form a uniformly conductive corona sheath. The formation of the corona sheath extends a radius a_{22} into the ambient air, i.e.

$$a_{22} = \frac{V}{E_{ABR} \cosh^{-1}\left(\frac{h}{a_{22}}\right)}, \qquad (3.16)$$

where V is the voltage drop from the corona sheath to ground and E_{ABR} (3MV/m) is the breakdown strength of air. The electric field used for determining the air conductivity σ (E) in the corona sheath is taken at midsheath, i.e.

$$E = \frac{V}{\left(\frac{a_{22}+a_2}{2}\right) \cosh^{-1}\left(\frac{h}{a_{22}}\right)}. \qquad (3.17)$$

From Figure 3.3, the per unit length resistance of the corona sheath, when formed, can be viewed as an annular ring with uniform conductivity $\sigma(E)$. In this model, strict retention of a three node transmission line formulation results in a corona sheath being perfectly conducting in the radial direction (which will be refined later).

3.2.3 Surface Cable Model with Corona

When an insulated cable is on the surface of a lossy ground, the soil medium must be included in the two conductor transmission line formulation. The three equation model of the previous study modelled the soil medium. In addition, the soil and dielectric nonlinearities were modelled. The two conductor transmission line model which includes air, soil, and dielectric nonlinearities is shown in Figure 3.4.

Most of the parameters in the two conductor transmission line model remain unchanged from the three equation transmission line model. However, the parameters specifying the second transmission line (i.e. corona sheath) require discussion. When the corona sheath forms it extends a radius a_{22} and is assumed to have a uniform conductivity $\sigma(E)$. Note that the corona sheath conductivity $\sigma(E)$ is a function of the electric field E which is in turn a function of the radial distance from the cable center.

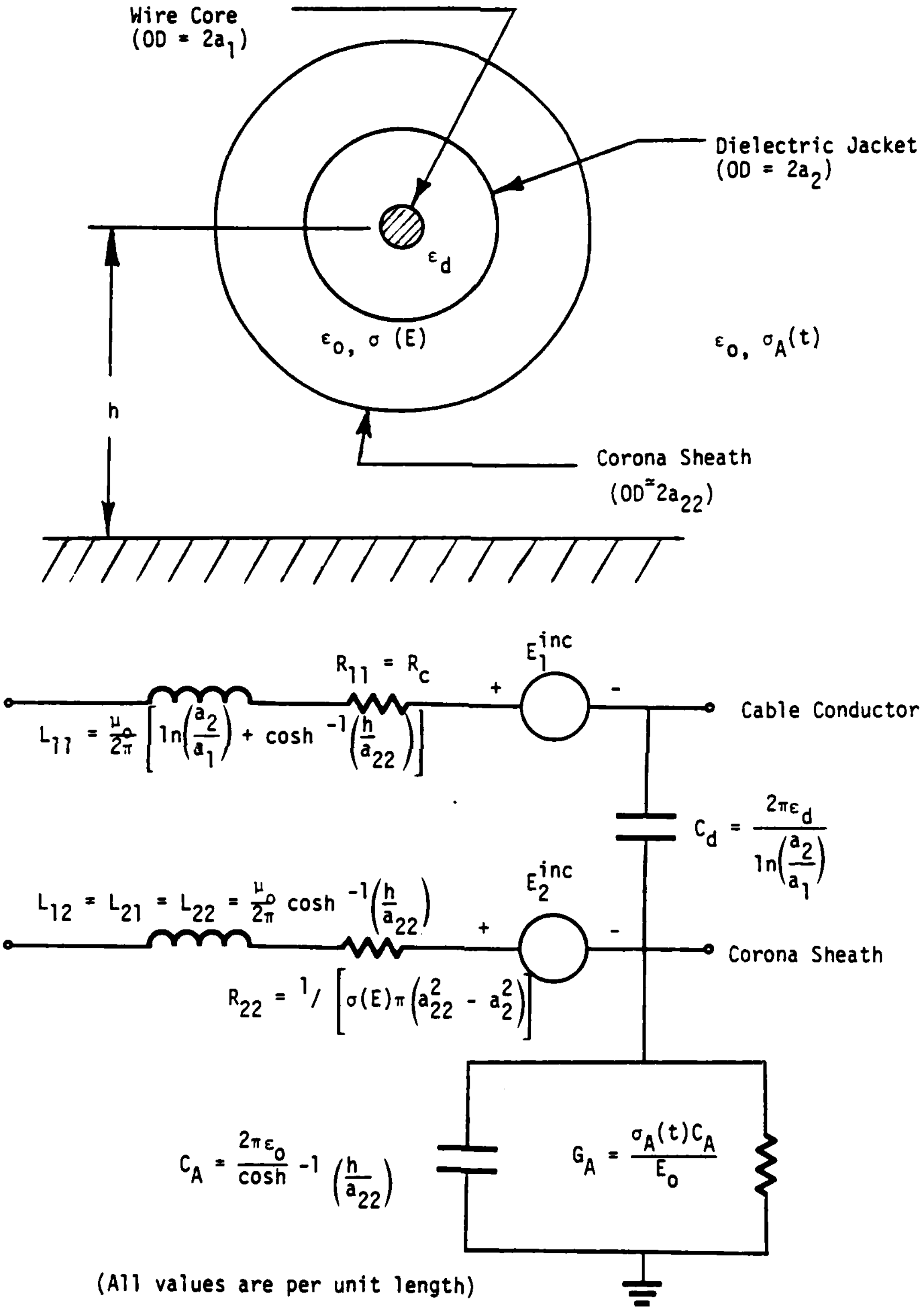

Figure 3.3 Geometry and Equivalent Transmission Line for an Insulated Wire Over a Perfectly Ground Plane. All elements are multiplied by the spatial increment Δz.

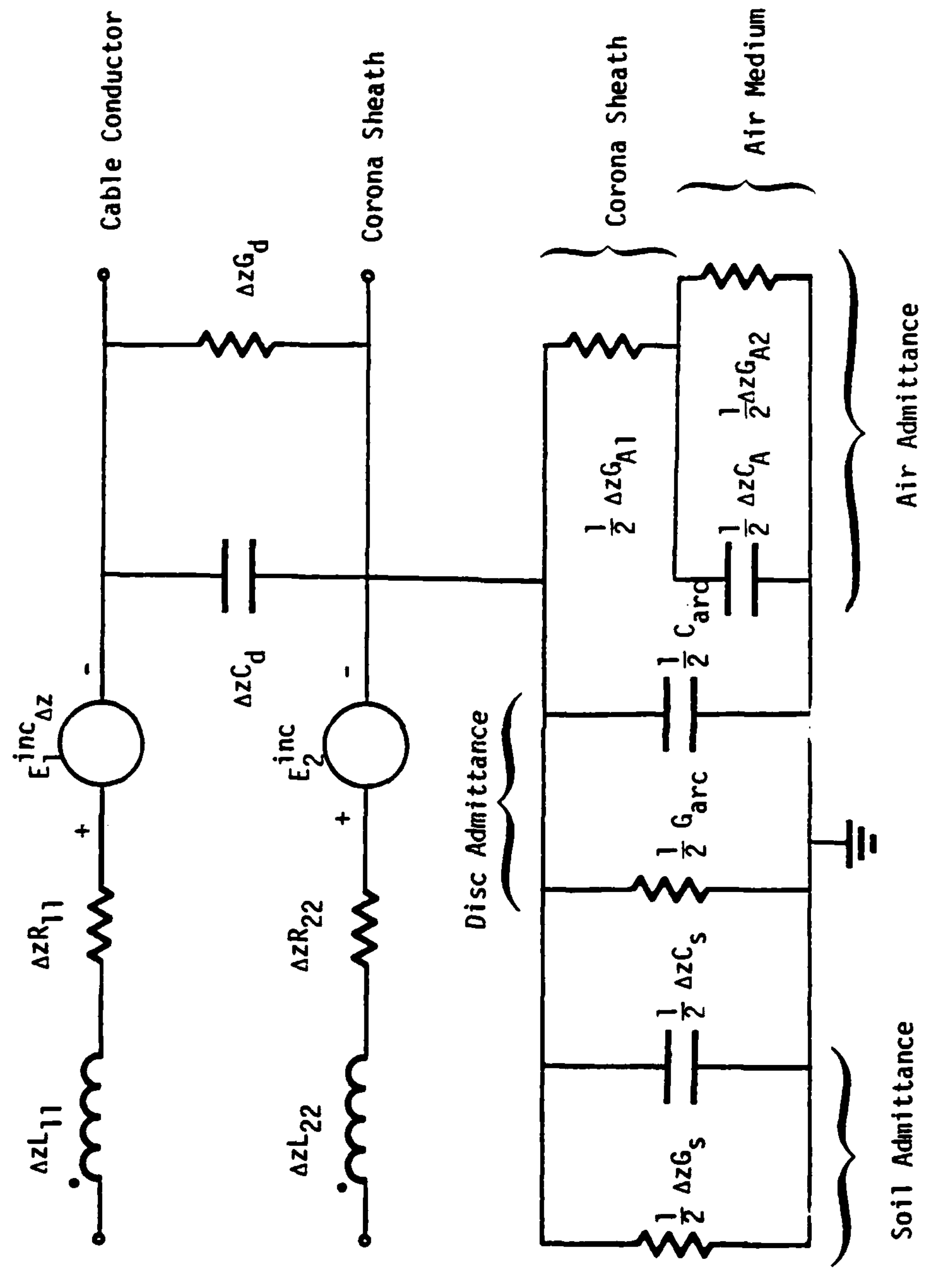

Figure 3.4 Surface Cable Model which Includes Air, Soil, and Dielectric Nonlinearities

The electric field used to compute the corona sheath conductivity is at midsheath [i.e. $(a_{22}-a_2)/2$]. On this basis, the per unit length impedance and admittance parameters for the second transmission line are determined.

The impedance per unit length for the two conductor transmission line is obtained from solutions to simpler problems. From the coaxial geometry, the per unit length inductance matrix elements are

$$L_{11} = \frac{\mu_o}{2\pi}\left\{\ln\left(\frac{a_2}{a_1}\right) + 2\ln\left(\frac{a_{31}}{a_{21}}\right)\ln\left(\frac{a_{32}}{a_{22}}\right) \Big/ \left[\ln\left(\frac{a_{31}}{a_{21}}\right) + \ln\left(\frac{a_{32}}{a_{22}}\right)\right]\right\} \text{, and} \tag{3.18}$$

$$L_{12} = L_{21} = L_{22} = \frac{\mu_o}{\pi}\ln\left(\frac{a_{32}}{a_{22}}\right) , \tag{3.19}$$

where the second subscript on the radii a_2 and a_3 differentiate between the soil (subscript 1) and air (subscript 2) media. Should the air not break down, the inductance of the cable equation 3.18 reduces to that obtained in the three equation transmission line formulation equation 3.8. When the corona sheath conducts, the axial current flows through the upper half of an annular ring formed in the air medium. This results in resistance per unit length matrix elements of

$$\left.\begin{aligned} R_{11} &= R_c \\ R_{12} &= R_{21} = 0 \\ R_{22} &= 2/\left[\sigma(E)\pi(a_{22}^2 - a_2{}^2)\right], \end{aligned}\right\} \tag{3.20}$$

where R_c is the DC resistance per unit length of the cable.

The corona sheath and surrounding air medium shown schematically in Figure 3.4 can be approximated as shown in Figure 3.5 which is valid over the frequency range of interest. This approximation is possible because of the large impressed air conductivity from the radiation source.

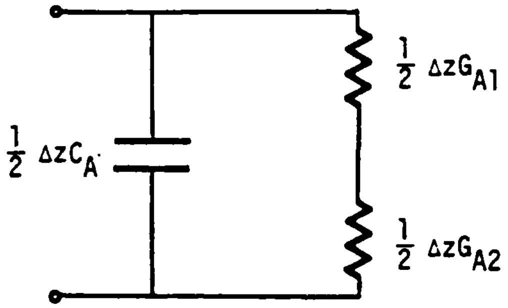

Figure 3.5 Approximation to Air Admittance of Figure 3.4

The circuit equivalent is used because an additonal node does not have to be incorporated in the numerical analysis as would be required for the circuit of Figure 3.4. This greatly saves computer resources.

The admittance per unit length is retained from the three equation transmission line model with the exception of the total per unit length air conductance and capacitance. The total air conductance per unit length obtained from Figure 3.5 is

$$G_A = \frac{G_{A1}\ G_{A2}}{G_{A1} + G_{A2}}, \tag{3.21}$$

where

$$G_{A1} = \frac{2\pi\ \sigma(E)}{\ln\left(\frac{a_{22}}{a_2}\right)} \tag{3.22}$$

and

$$G_{A2} = \frac{2\pi\sigma_A(t)}{\ln\left(\frac{a_{32}}{a_{22}}\right)}, \tag{3.23}$$

where $\sigma_A(t)$ is the impressed air conductivity, G_{A1} corresponds to the corona sheath, and G_{A2} corresponds to the air medium. The conductance per unit length matrix elements become (see Figure 3.2)

$$G_1 = G_d \tag{3.24}$$

$$G_2 = \frac{1}{2}\left[G_A + G_s\left(1 - \frac{r_{arc}}{\Delta z/2}\right) + \frac{G_{arc}}{\Delta z}\right] , \tag{3.25}$$

where G_s is the soil conductance per unit length defined in equation 3.7, G_{arc} is the conductance of the arc defined in equation 3.1, and G_d is the dielectric conductance (zero before and "infinite" after dielectric breakdown). The capacitance per unit length matrix elements are (see figure 3.2)

$$C_1 = C_d \tag{3.26}$$

$$C_2 = \frac{1}{2}\left[C_A + C_s\left(1 - \frac{r_{arc}}{\Delta z/2}\right) + \frac{C_{arc}}{\Delta z}\right] , \tag{3.27}$$

where C_d is the per unit length capacity of the dielectric defined in equation 3.10, C_A and C_s are the respective per unit length capacities of the air and soil defined in equation 3.5, and C_{arc} is the arc capacity defined in equation 3.2. Actually the soil and air can break down. This allows the radii of the corona sheath and soil to vary. A more accurate representation of the air and soil capacities per unit length should be

$$C_A = \frac{2\pi\epsilon_o}{\ln\left(\frac{a_{32}}{a_{22}}\right)} \quad \text{and } C_s = \frac{2\pi\varepsilon_s}{\ln\left(\frac{a_{31}}{a_{21}}\right)} \tag{3.28}$$

where the second subscript 2 refers to the air medium and the second subscript 1 refers to the soil medium.

The voltage induced electric field is determined from the soil voltage V_s, corona sheath conductance, and air medium conductance at the radius of interest r. The electric field within the corona sheath (used to compute $\sigma(E)$) is

$$E(r) = \frac{V_s}{r\left[\ln\left(\frac{a_{22}}{a_2}\right) + \frac{\sigma(E)}{\sigma_A(t)} \ln\left(\frac{a_{32}}{a_{22}}\right)\right]} \tag{3.29}$$

whereas the electric field in the air medium outside the corona sheath is

$$E(r) = \frac{V_s}{r\left[\frac{\sigma_A(t)}{\sigma(E)} \ln\left(\frac{a_{22}}{a_2}\right) + \ln\left(\frac{a_{32}}{a_{22}}\right)\right]} \tag{3.30}$$

Conversely if the electric field is known, the radius can be determined. Air breaks down when the electric field exceeds 3MV/m. Using this electric field strength, the corona sheath radius is

$$a_{22} = \frac{V_s}{E_{ABR}\left[\frac{\sigma_A(t)}{\sigma(E)} \ln\left(\frac{a_{22}}{a_2}\right) + \ln\left(\frac{a_{32}}{a_{22}}\right)\right]}, \tag{3.31}$$

where E_{ABR} is the breakdown strength of air. It should be noted that to solve the transcentental equation 3.31 exactly at every time step and location on the cable is a time consuming process. However, an approximate solution can be obtained by using the values of a_{22} from the previous time step on the right-hand side of the equation to find the new values of a_{22} on the left-hand side of equation 3.31. This method of solution is appropriate for the process of corona sheath growth. However, instantaneous corona sheath growth and decay is not physically possible. The corona sheath radius is moderated in the growth and decay processes. For corona growth, the conductivity within the corona region must be great enough for a sheath to physically form. The corona sheath radius is moderated by the corona conductivity shown in Figure 3.6. For corona decay, the corona sheath radius is allowed to decay by 10% of its radius calculated from the previous time step.

Refinement of the surface cable model to allow for radial current flow through the corona sheath is possible in the two conductor three node transmission line formulation. Because any radial current flow through the

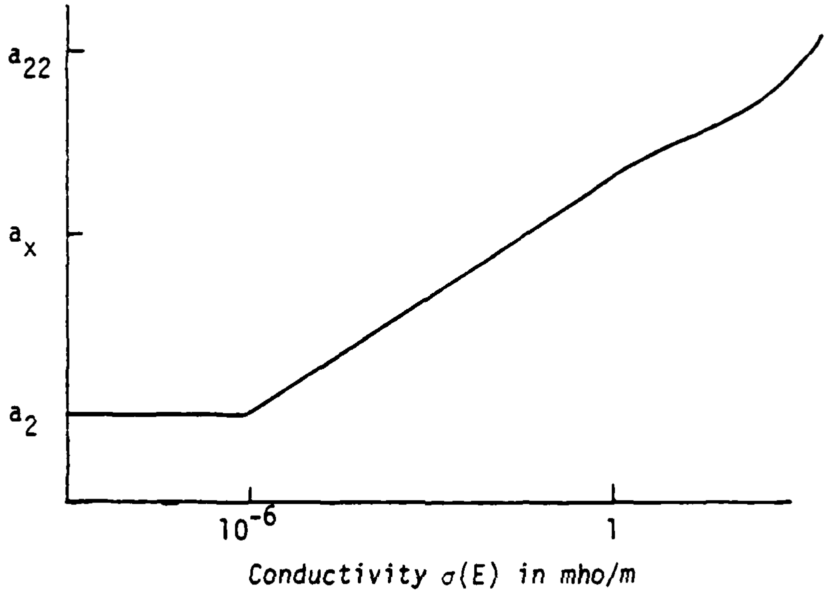

where $a_x = a_2 + (a_{22} - a_2)\,\sigma(E)$ for $\sigma(E) < 1$

$a_x = a_{22}$ for $\sigma(E) > 1$

Figure 3.6 Corona Sheath Growth Moderation Scheme air medium must also flow through the corona sheath, the voltage drop across the air or corona sheath can be expressed in terms of the soil voltage (i.e. voltage across the corona sheath and air medium). By knowing the voltage drop and distance, the voltage induced electric field in either the air medium or corona sheath is determined in terms of the conductance of the corona sheath (equation 3.22) and air medium (equation 3.23).

CHAPTER IV

RESULTS OF SURFACE CABLE COMPUTATIONS

4.1 Background

In order to establish the significance of air breakdown on the surface cable response, several case studies are performed.

These studies include:

1) Wire over a lossless ground plane,
2) Surface cable with and without nonlinearities,
3) Comparison of results with those of the previous study reported in Reference 1,
4) Angle of Incidence Parameter Study, and
5) High Altitude EMP (HEMP) and surface cable.

From these studies the effects of air breakdown on the cable response are evaluated.

4.2 Insulated Wire Over a Lossless Ground Plane

The first configuration studied is that of an insulated wire over a lossless ground plane. This case is examined first because of the problem's relative simplicity. The corona effects in this case can be studied without having to account for earth losses, impressed time varying air conductivity, and other nonlinearities.

The problem is illustrated in Figure 4.1. The wire is 50m long and shorted to ground on the left end. Cable response was studied for normal and end on angles of incidence.

For normal incidence, the incident electric field is given in Figure 4.2 and is parallel to the wire. The midcable responses of wire current and voltage are given in Figures 4.3 and 4.4, respectively. It is noted that the effect of the corona is to create a rather narrow (≈ 16ns, full width) current pulse of significant amptitude which adds to the original (linear) pulse, and to create a similar voltage pulse which subtracts from the original pulse. These pulses can be interpreted as coming from charge which is used to create the corona sheath, and as the sheath radius and current increase, the voltage decreases in order that energy may be conserved.

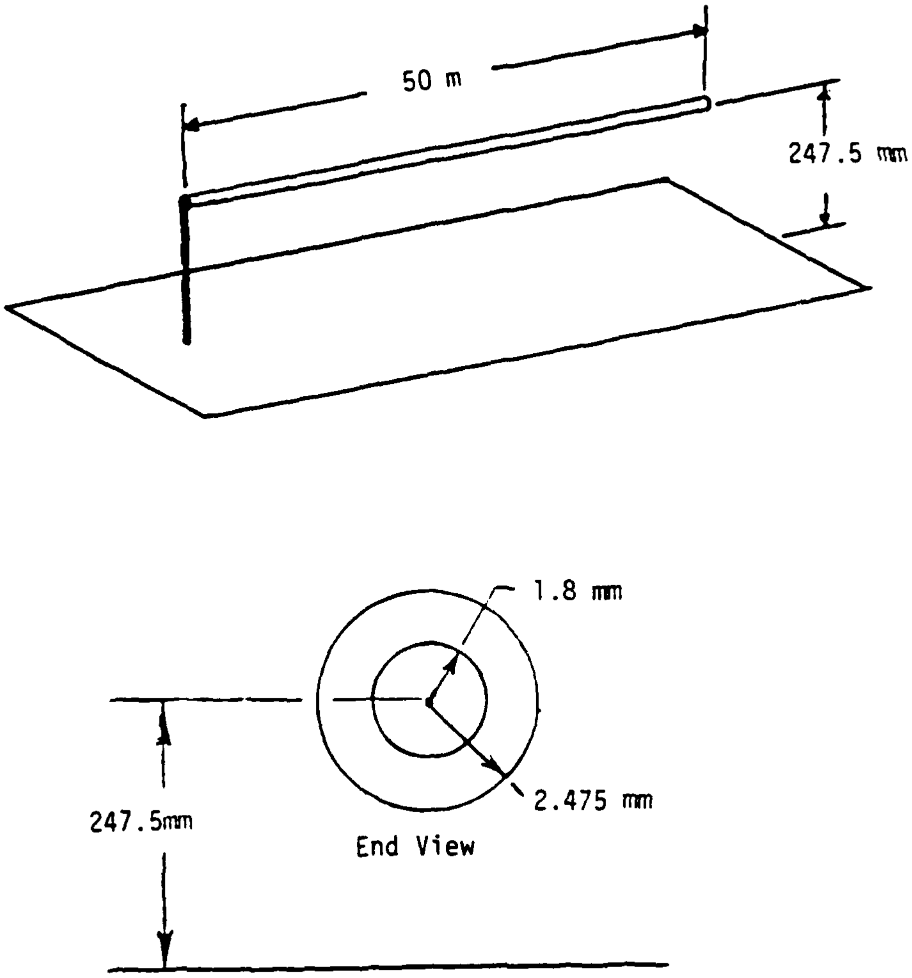

Figure 4.1 Wire Over a Lossless Ground Plane

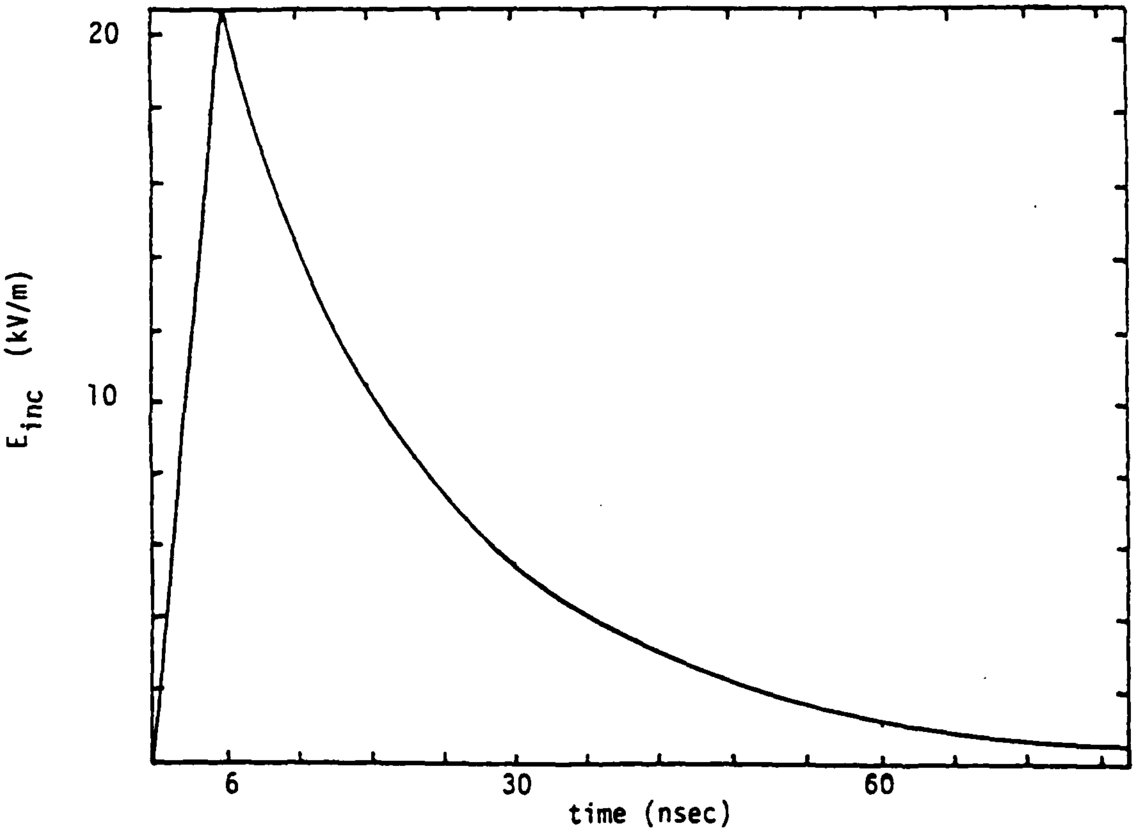

Figure 4.2 Incident Electric Field for Normal Incidence and Incidence from the Open End

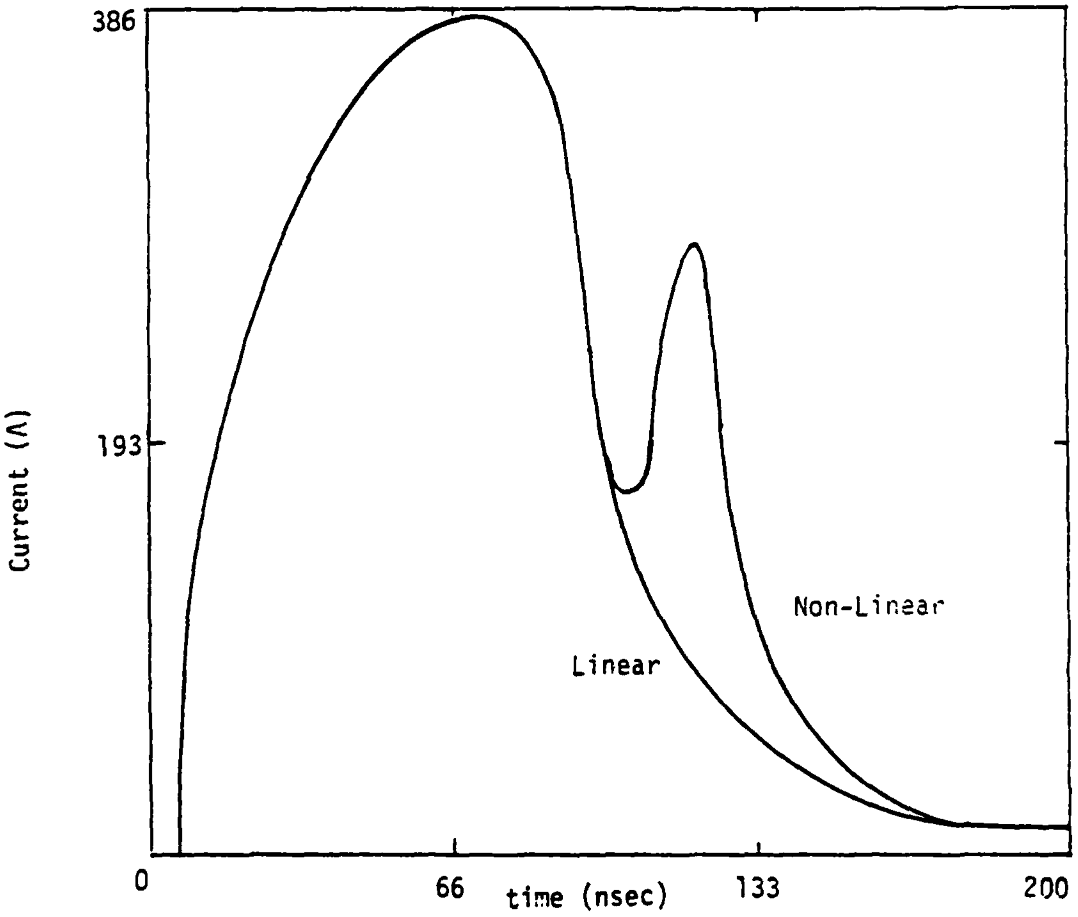

Figure 4.3 Overlay of Linear and Non-Linear Midcable Current for Normal Incidence

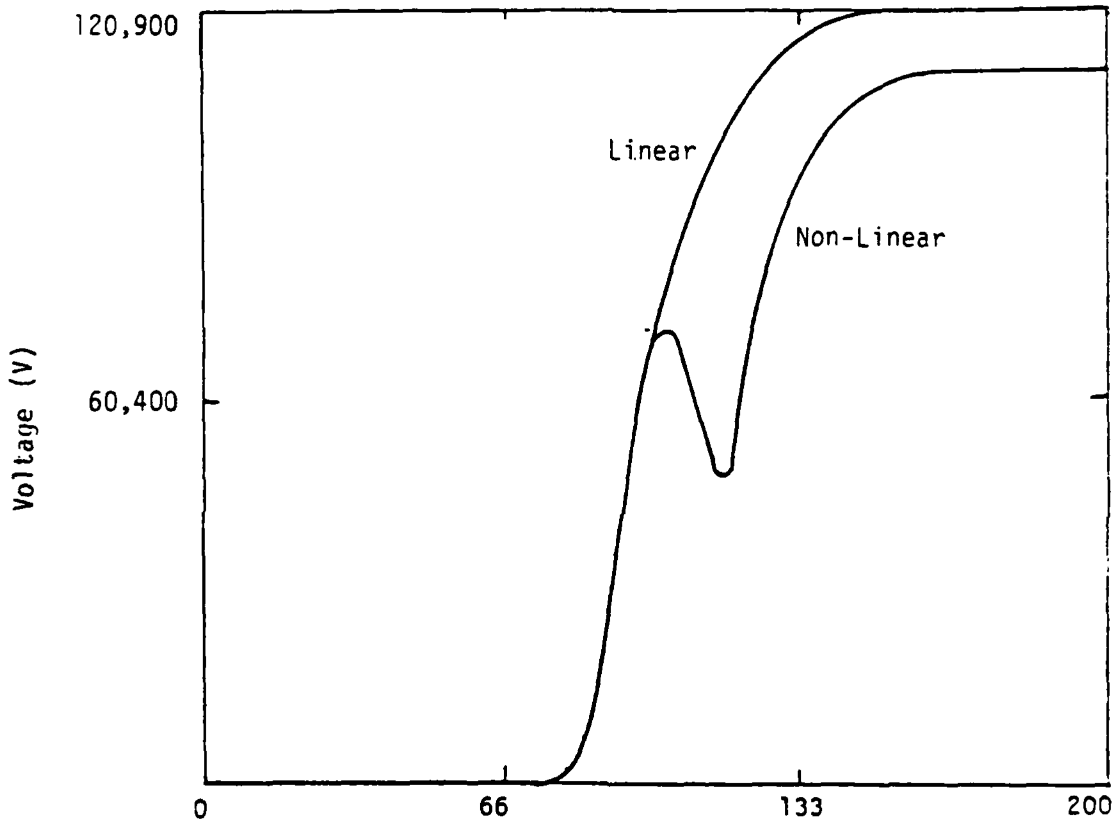

Figure 4.4 Overlay of Linear and Non-Linear Midcable Voltage for Normal Incidence

Because the cable voltage is zero at any point on the line until a time equal to the transit time from the open end, the pulse travels from the open end to the shorted end. Figures 4.5 and 4.6 show the corona sheath radius and conductivity at the open end of the cable. In this case, the radius expands to about 3.6 times the radius to the edge of the dielectric insulation, and the conductivity is on the order of a few hundred mhos/m. It takes about 26 ns for the corona sheath to form. The sheath radius grows and decays according to the induced voltage.

Results are also calculated for an electric field incident on the cable at the velocity of light from either the open or shorted end.

The electric field incident on the open end is shown in Figure 4.2 while the electric field incident on the shorted end is given in Figure 4.7.

Results for the case in which the field is incident from the shorted end are given in Figure 4.8 - 4.11. At a distance of 1/3 of the way down the cable, the effect of corona is to increase the current and decrease the voltage by only 8%. At the shorted end, the corona effects are more pronounced in that the short circuit current is increased by 24%. No significant changes in the waveshape are noticed. As shown in Figure 4.11, the corona sheath average conductivity is on the order of a few hundred mhos/m.

Midcable current and voltage responses are given in Figure 4.12 and 4.13 for incidence from the open end. The effect of corona is to increase the current by 26% and reduce the voltage by 7%. The oscillations evident in the responses are caused by numerical instabilities.

In general, for insulated wires over a perfect ground plane, it can be said that corona effects depend upon the angle of incidence. The main effect of including corona is to moderately increase the currents and decrease the cable voltages with respect to a linear analysis.

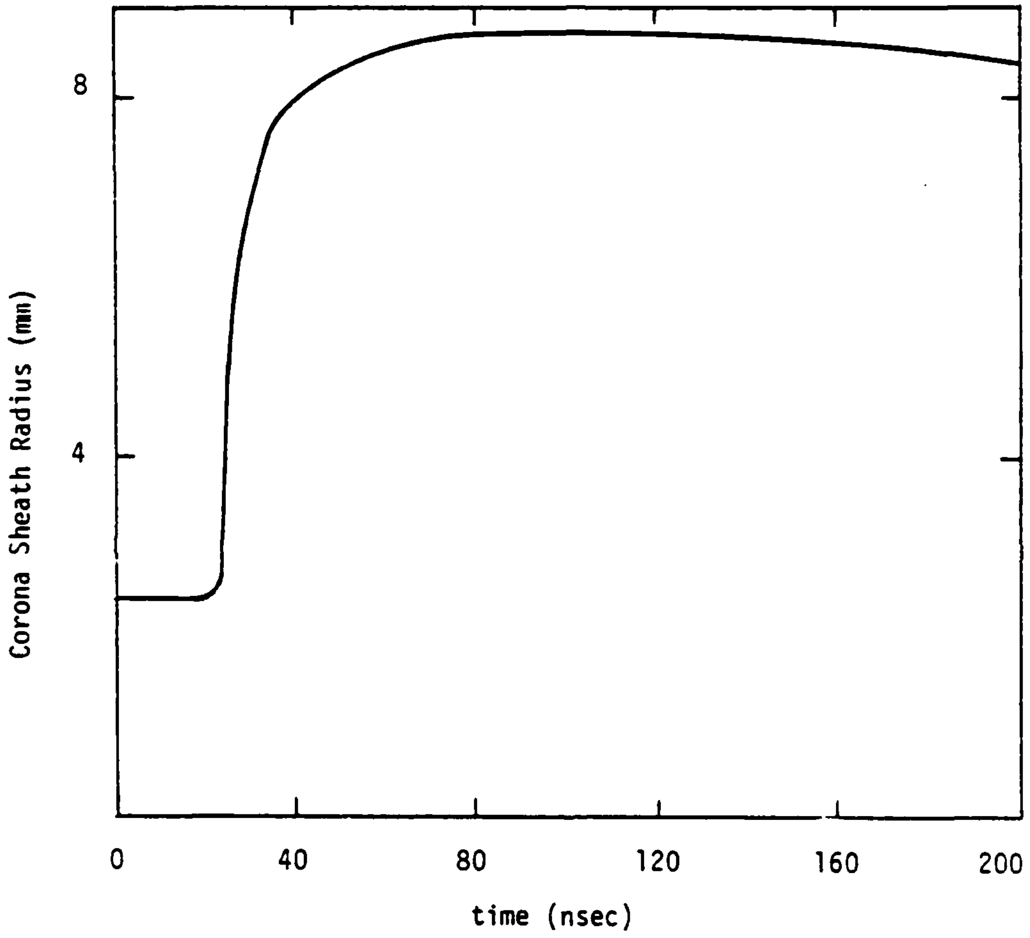

Figure 4.5 Corona Sheath Radius on Open End

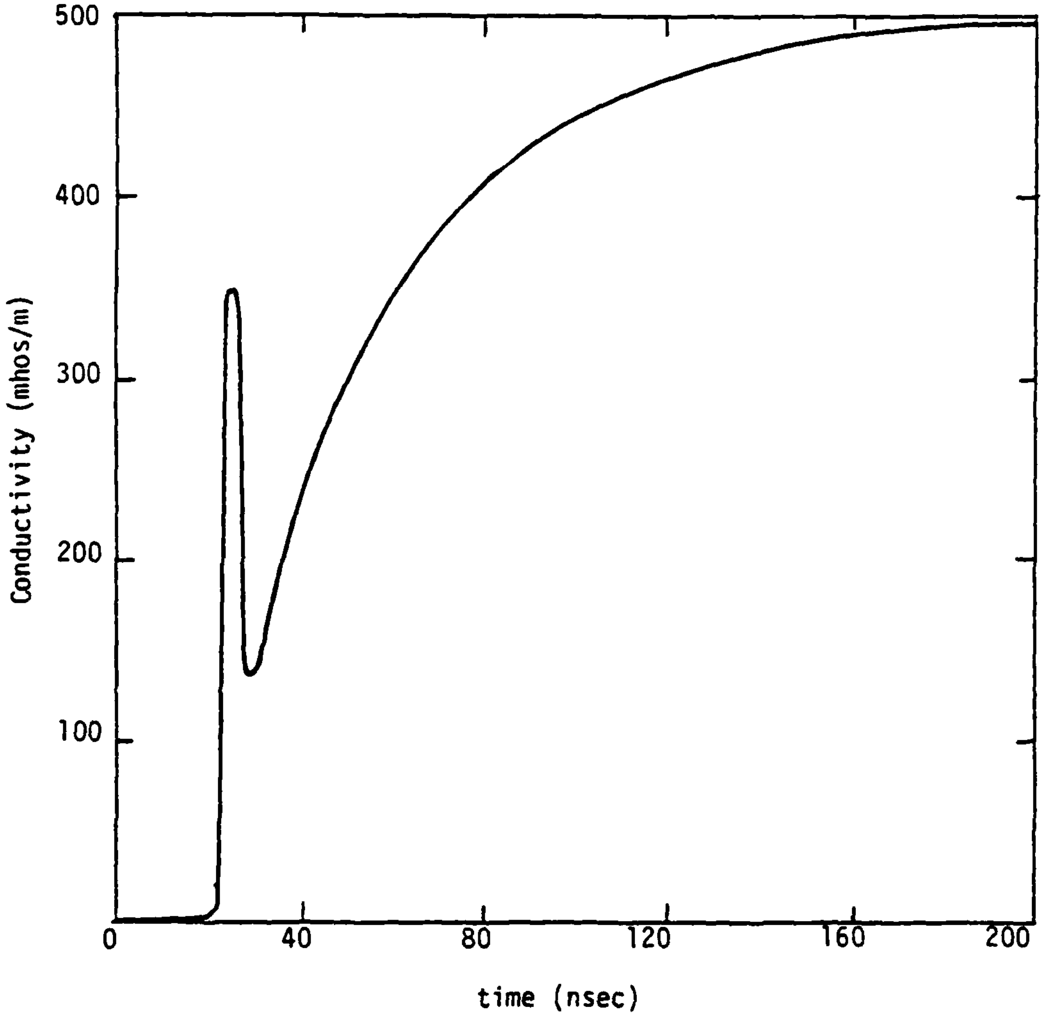

Figure 4.6 Air Conductivity in Corona Sheath on Open End

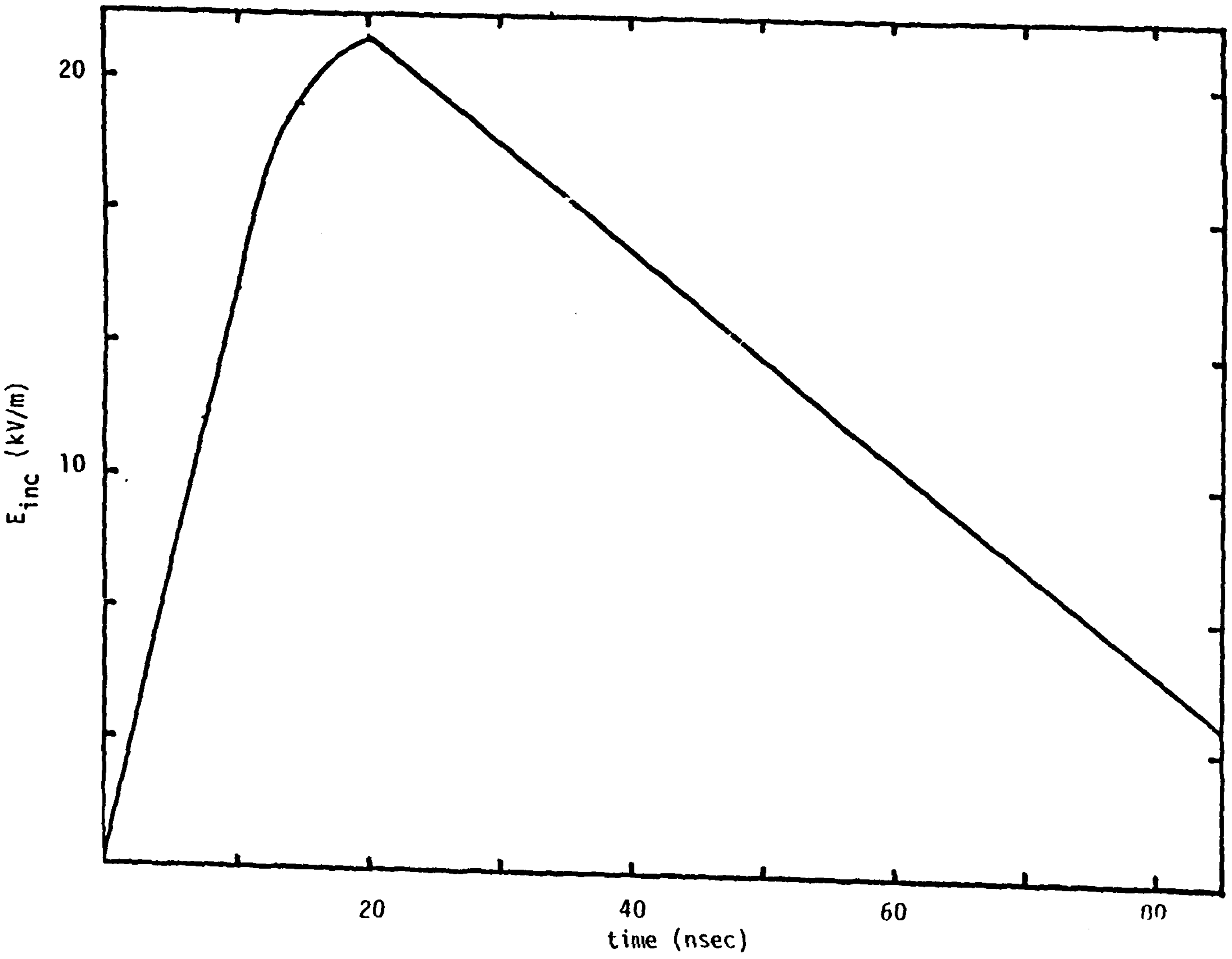

Figure 4.7 Electric Field Incident on Shorted End

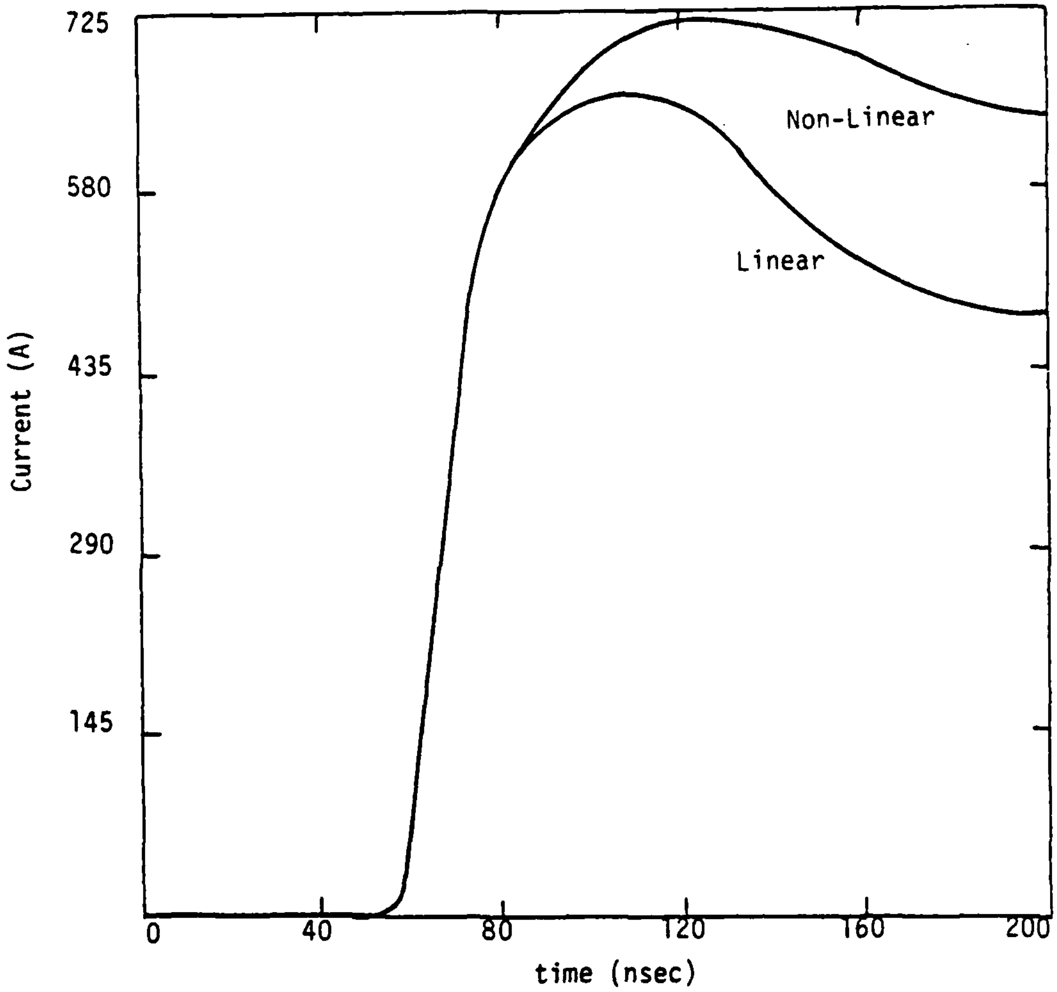

Figure 4.8 Linear and Non-Linear Current Response at 16.5 Meters From the Shorted End for Incidence From the Shorted End

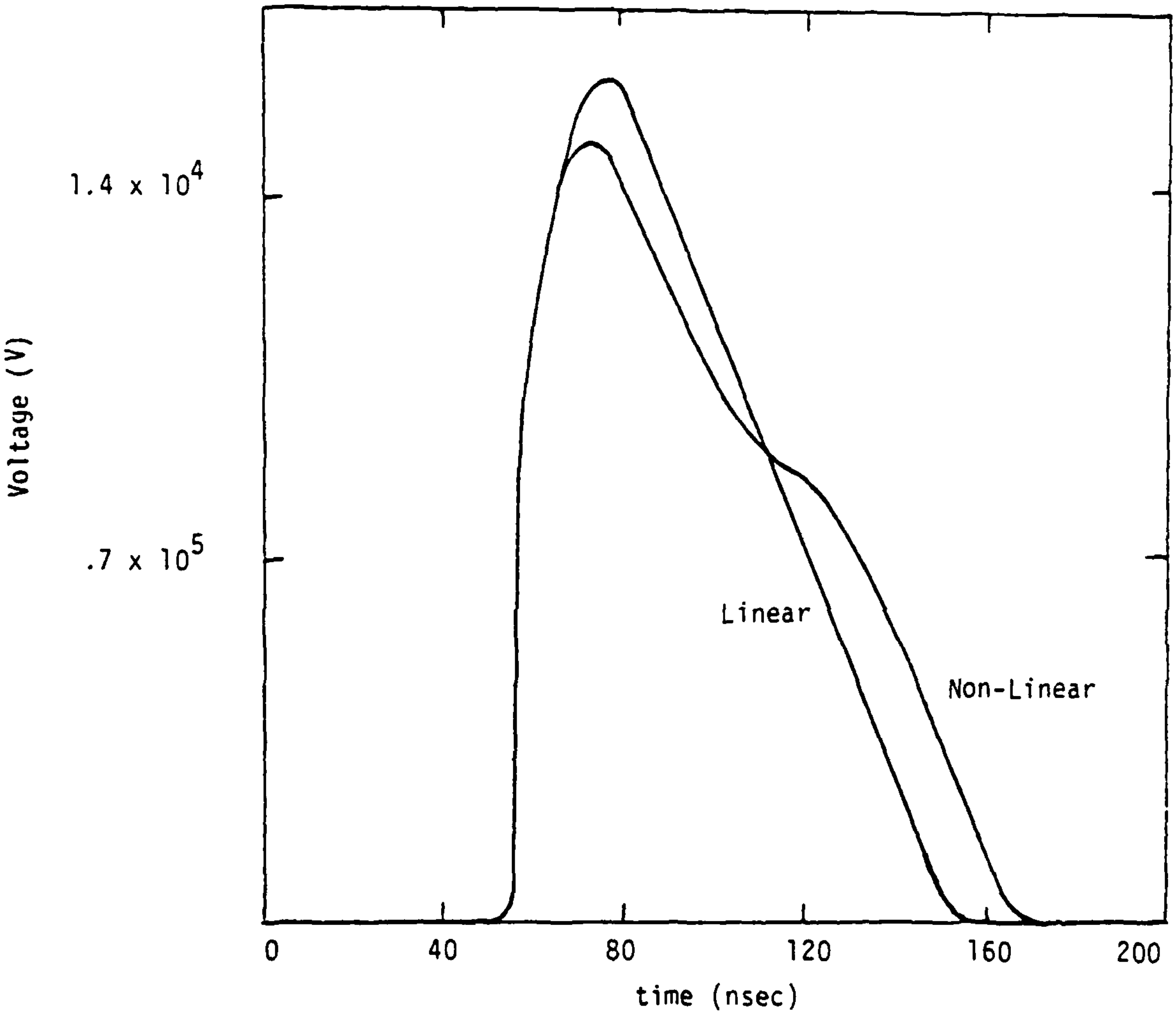

Figure 4.9 Linear and Non-Linear Voltage Response at 16.5 Meters From the Shorted End for Incidence From the Shorted End

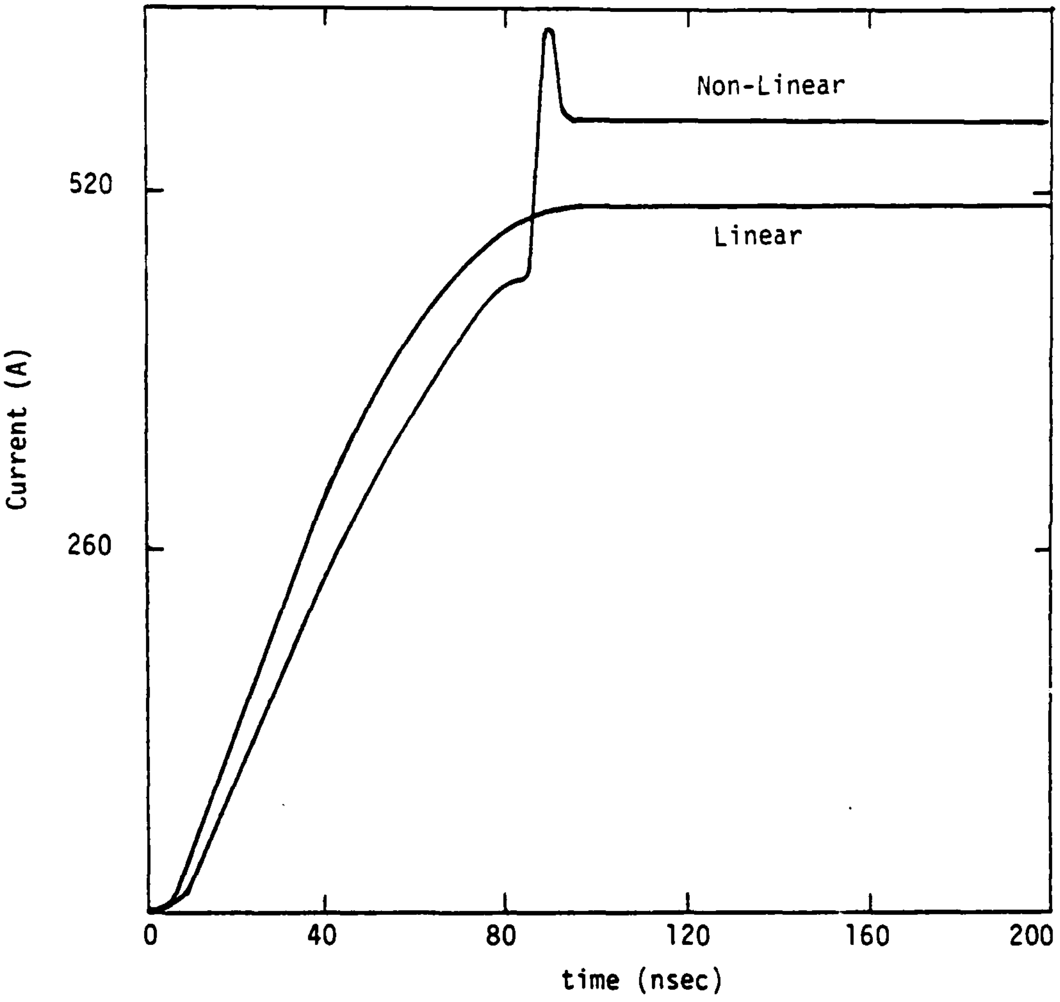

Figure 4.10 Linear and Non-Linear Short Circuit Current Response for Incidence from the Shorted End

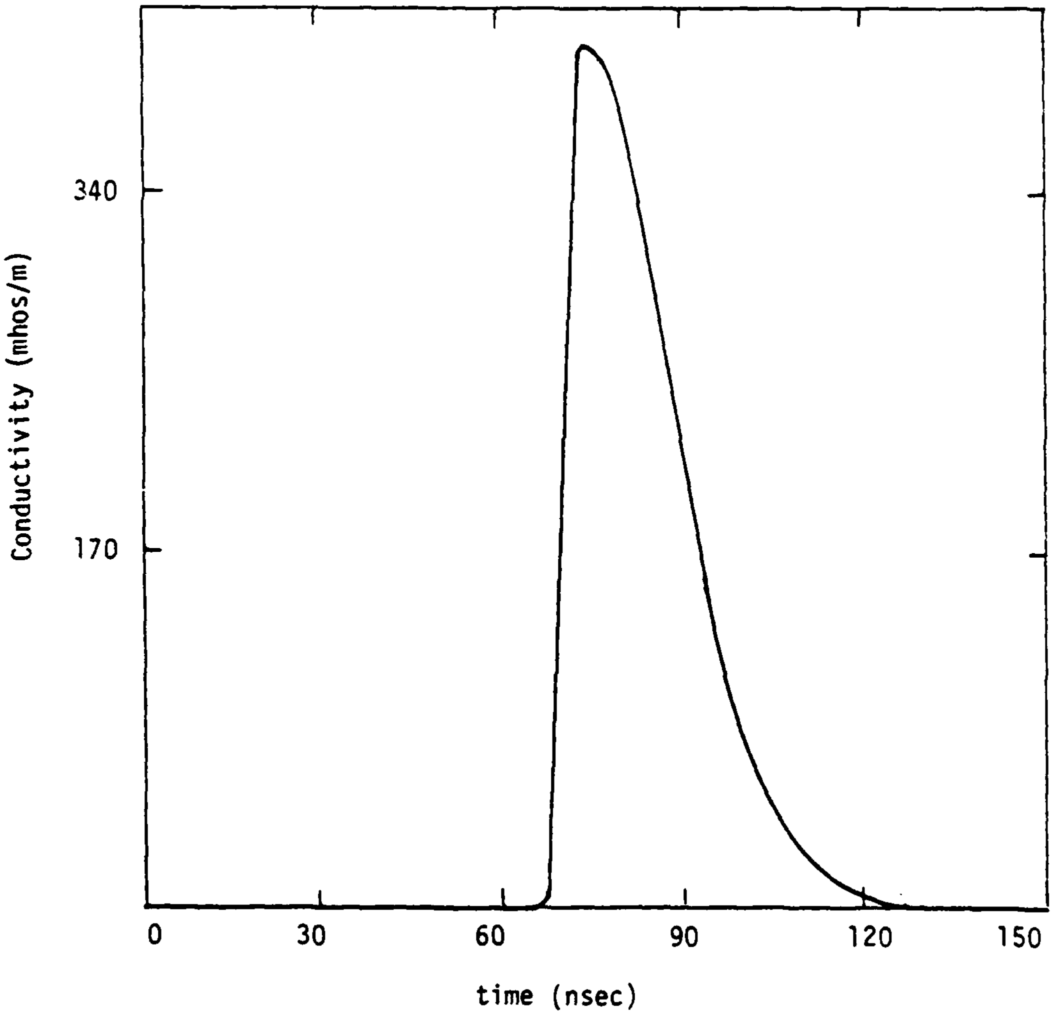

Figure 4.11 Corona Sheath Conductivity at 16.5 m From the Shorted End for Incidence From the Shorted End

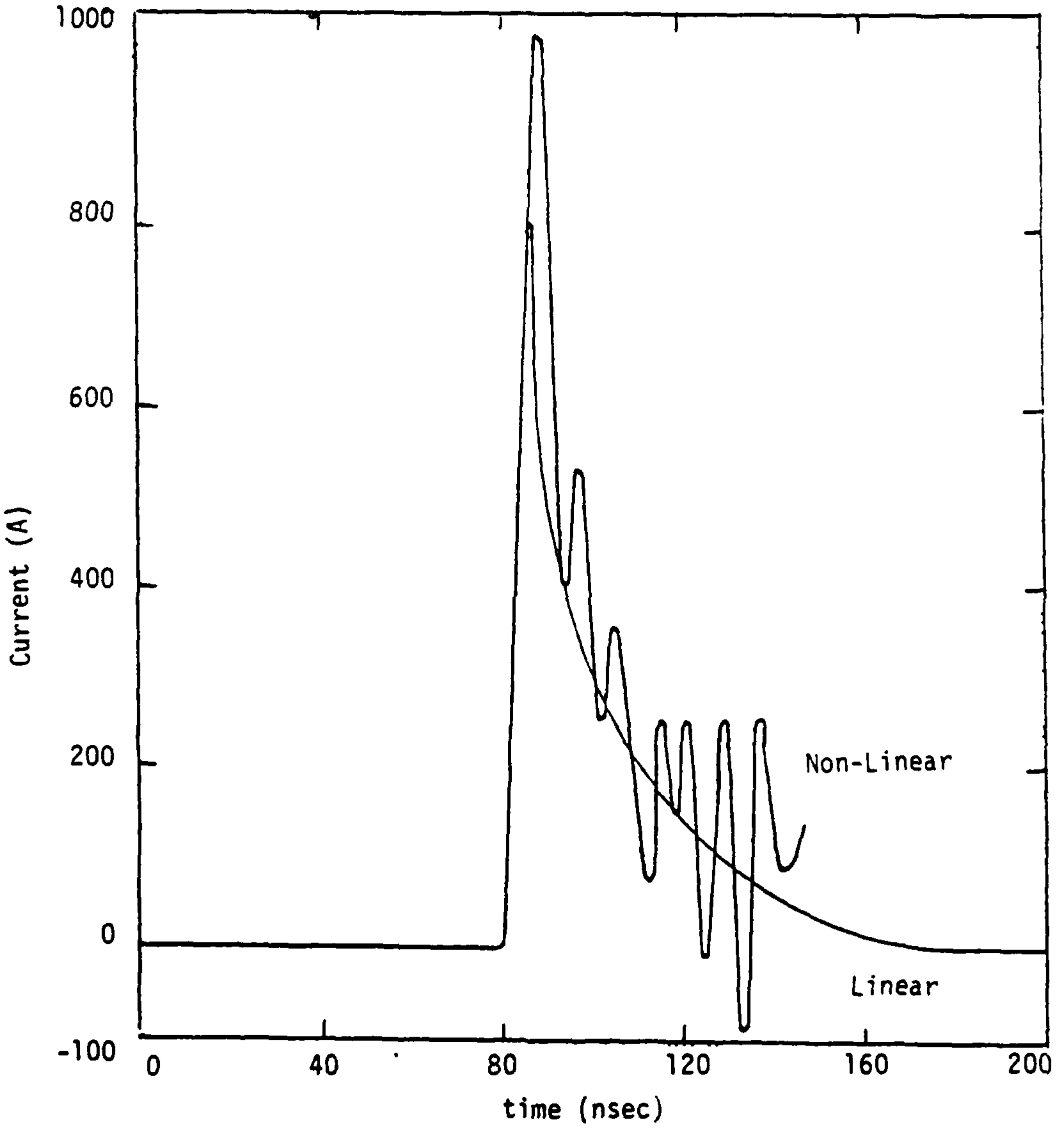

Figure 4.12 Overlay Linear and Non-Linear Midcable Current Response for Incidence From the Open End

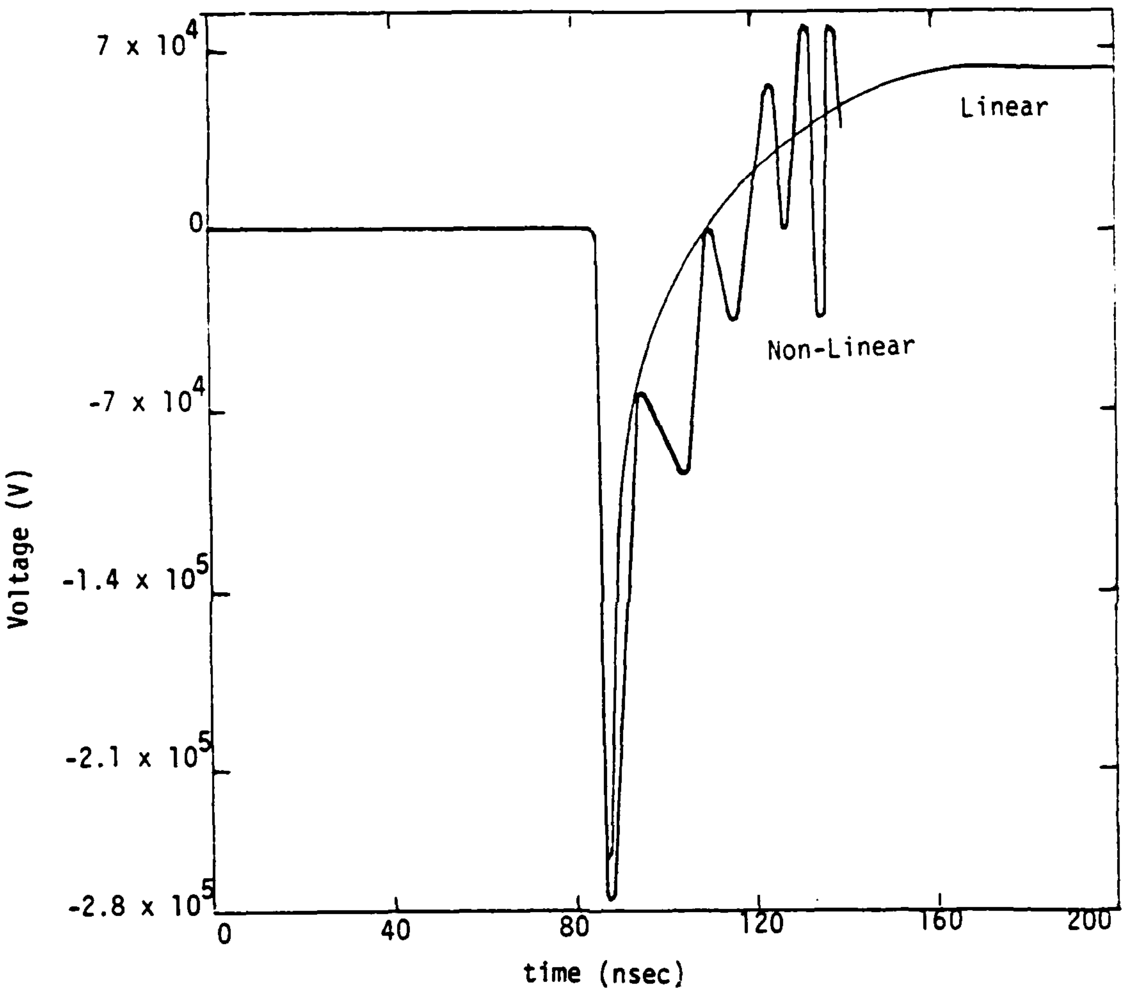

Figure 4.13 Overlay of Linear and Non-Linear Midcable Voltage Response for Incidence from the Open End

4.3 Linear and Non-Linear Response of Surface Cable

In general, there are three non-linear processes included in the surface cable model; soil breakdown, air breakdown, and dielectric breakdown. Cable responses which accounted for these processes separately and collectively were calculated and compared so that the importance of each process could be identified.

The cable studied consists of the outer shield and insulating jacket of RG-8. The inner conductor was not considered. Therefore the currents predicted in this study are the external shield currents of the RG-8. The cable is 600 m long and lies on the surface of the earth whose conductivity is .005 mho/m. It is in a tactical source region environment such that the cable is oriented radially to the source and spans the range from 400 m to 1000 m. The cable is open circuited at the end closest to the source and short circuited at the far end.

The tactical electromagnetic environment is a function of range. The radial electric field, impressed air conductivity, and the ionization rate are given in Figures 4.14, 4.15, and 4.16, respectively. The electric field and air conductivity used in the previous study [1] are also shown, and will be referred to later.

The results for the non-linear parameter study are shown in Figures 4.17 - 4.21. All of these results account for the impressed time varying air conductivity. It was found that including corona and soil breakdown did not noticeably change the cable response - results accounting for these two non-linear processes virtually overlay the linear responses. This effect in regard to the soil non-linearity was also noticed previously [1].

The only non-linear process that makes any difference is the dielectric breakdown. This is only observed near the open end, and no effect is observed at midcable or the far end. This is principally because the excitation contains very little low frequency content, and the high frequency energy is rapidly attenuated along the cable because of the lossy soil and conducting air. The results in Figures 4.17 and 4.18 show that dielectric breakdown makes no difference in response during this early time period. However, in Section 4.5, results are calculated to 30 μsec which do show that the late time current is increased by the dielectric breakdown.

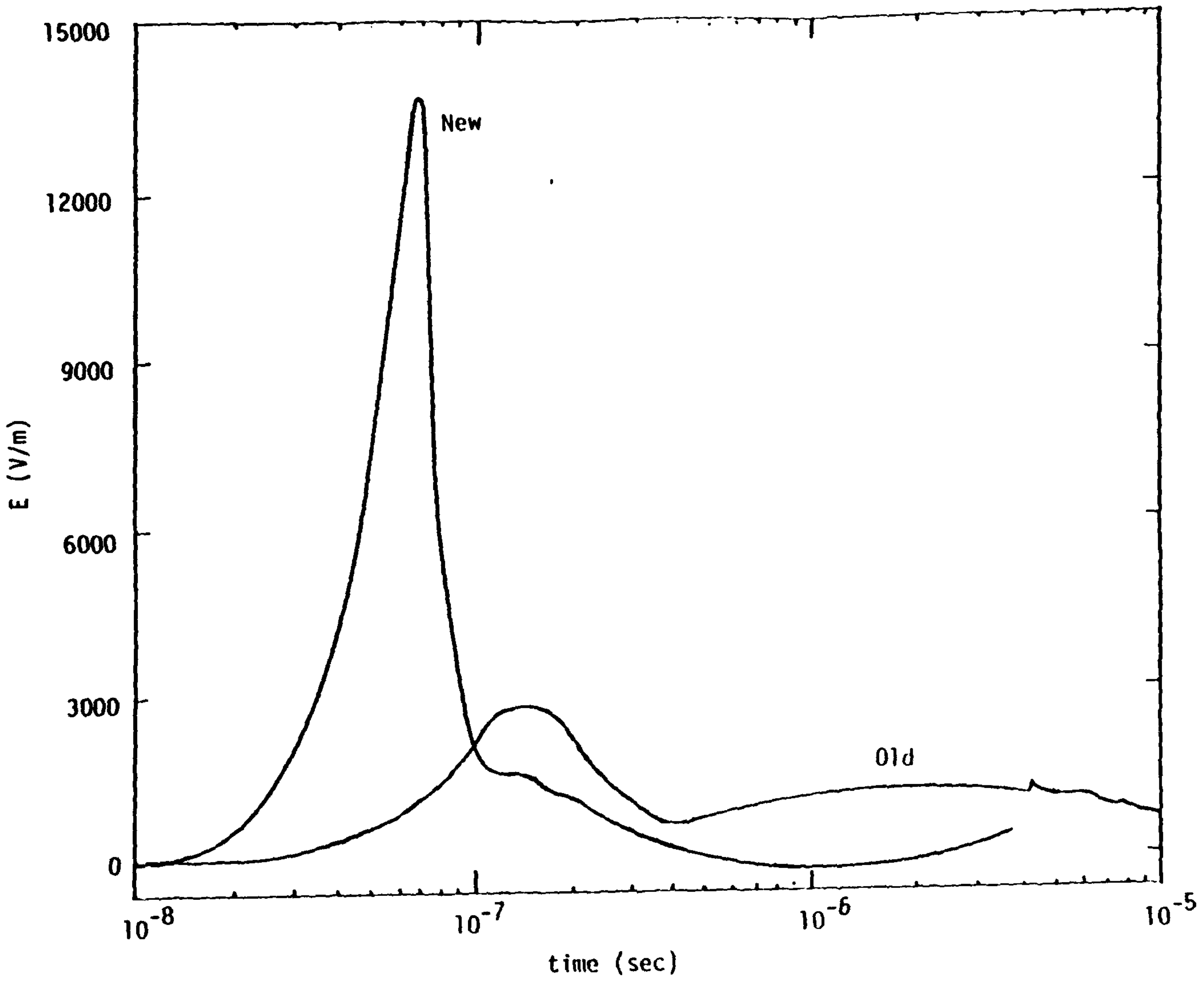

Figure 4.14 Tactical Radial Electric Field at 1000 m Range

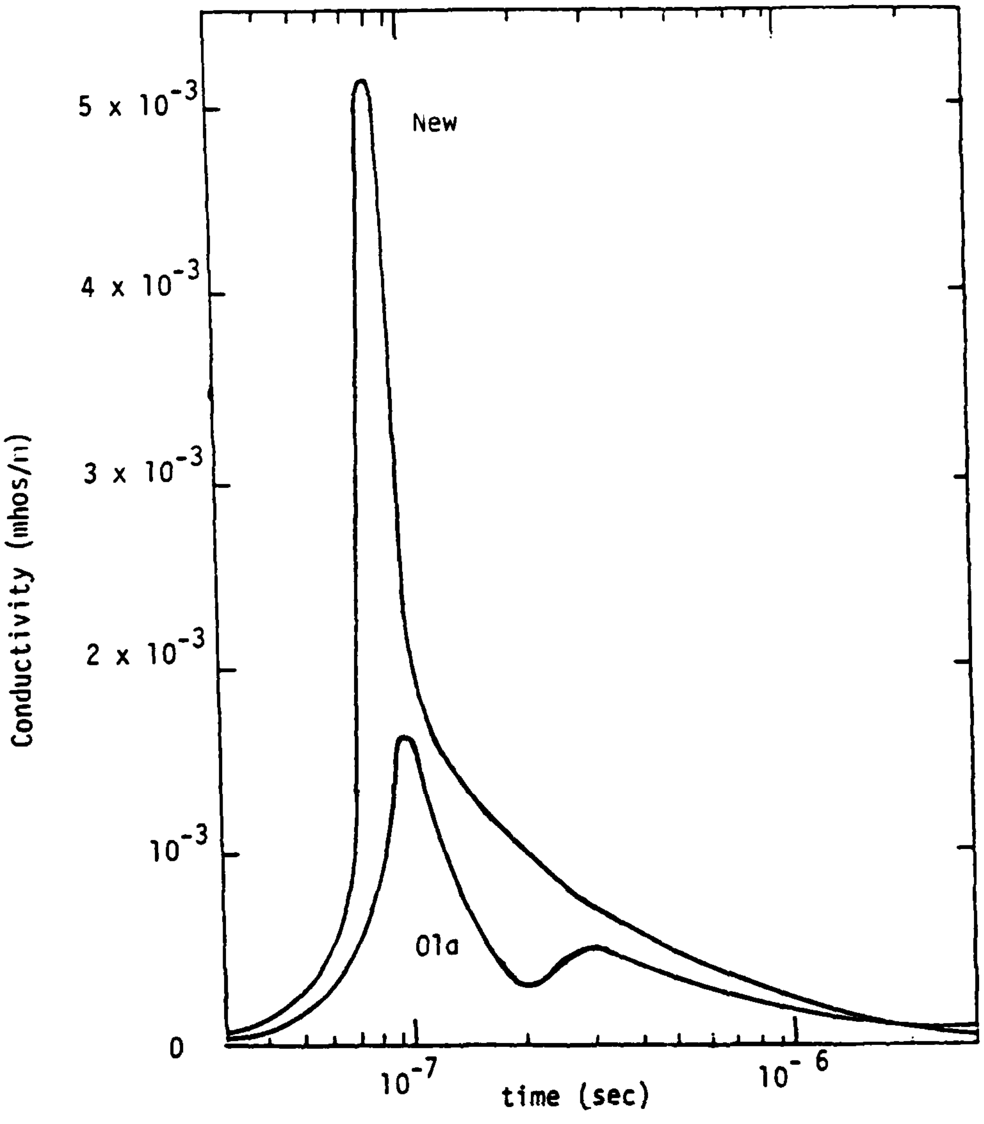

Figure 4.15 Tactical Air Conductivity at 1000 m Range

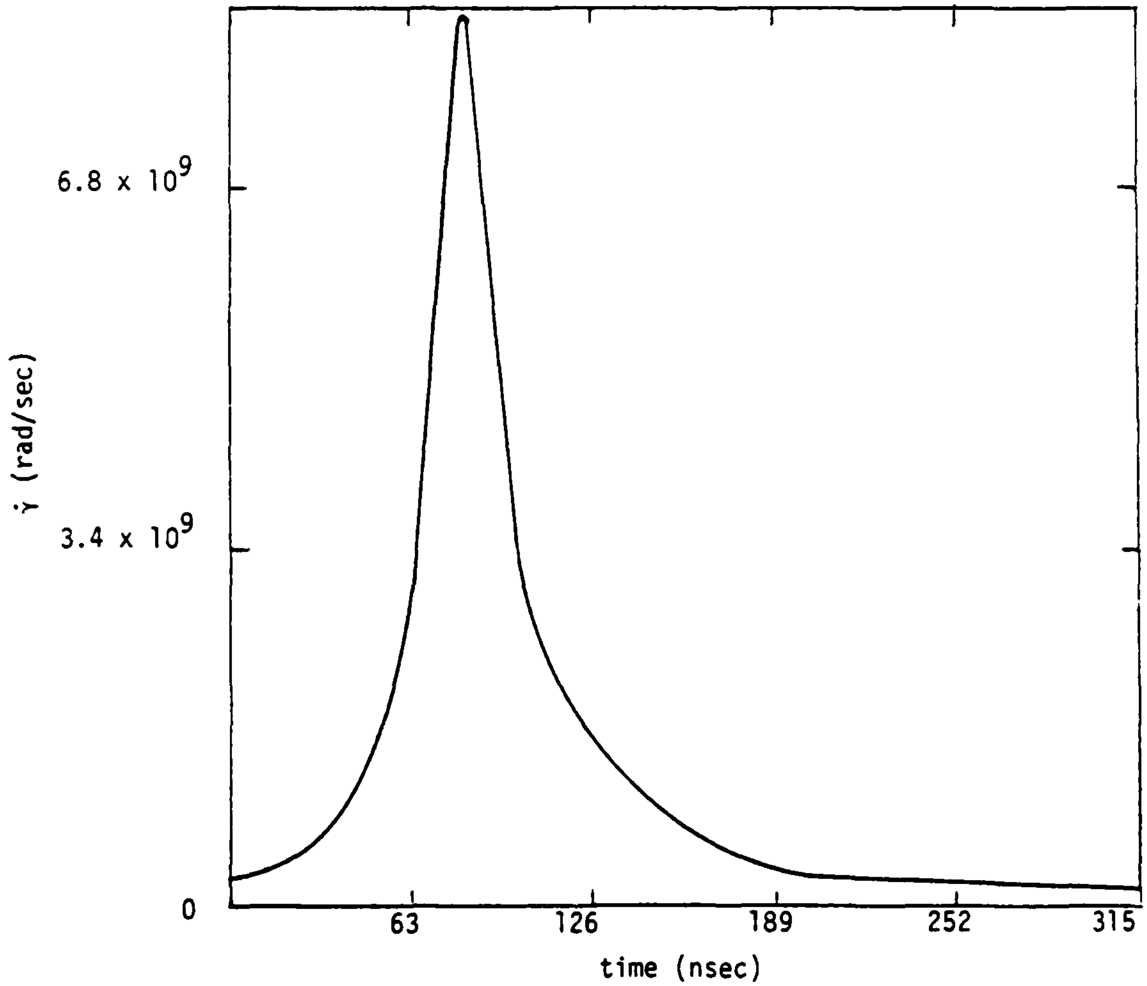

Figure 4.16 Ionization Rate at 1000 m Range

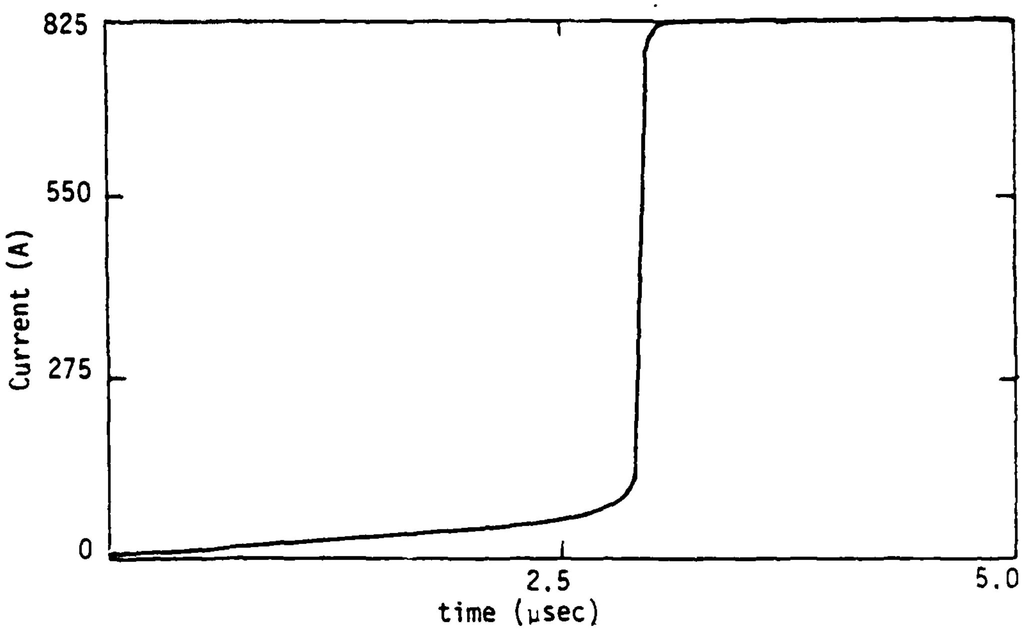

Figure 4.17 Short Circuit Current for Linear and Non-Linear Dielectric

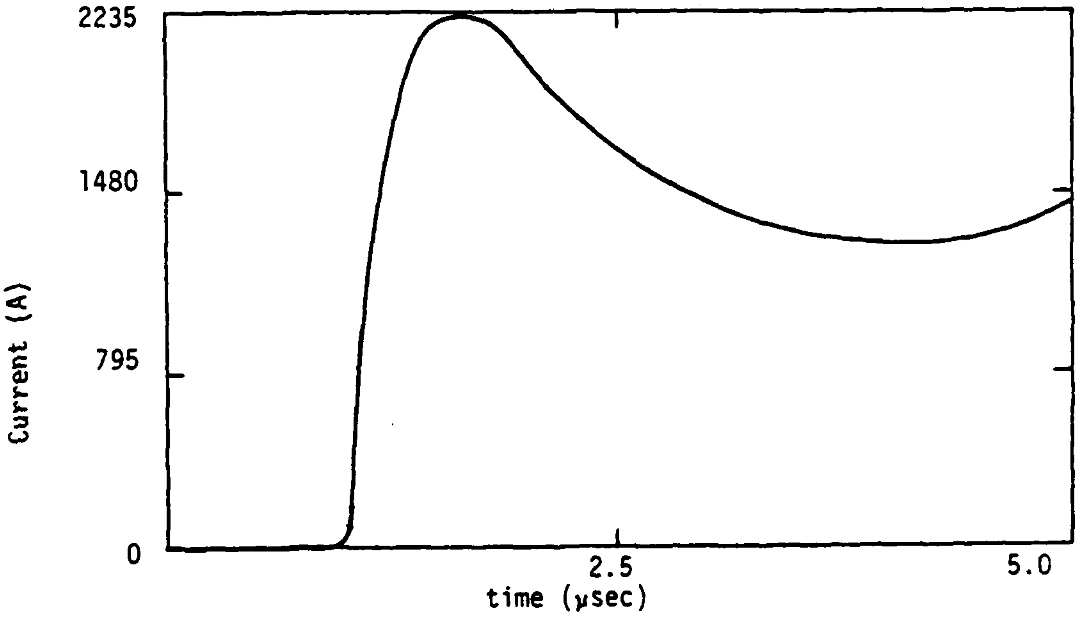

Figure 4.18 Midcable Current for Linear and Non-Linear Dielectric

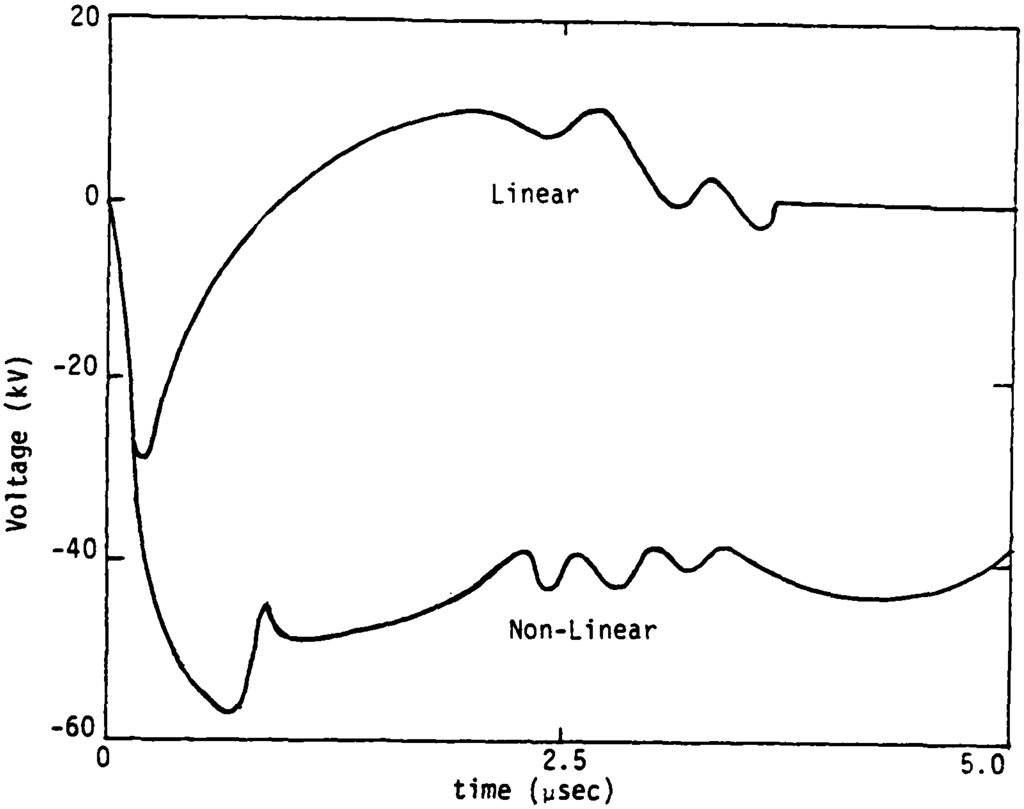

Figure 4.19 Overlay of Linear and Non-Linear Soil Voltage on Open End of Cable

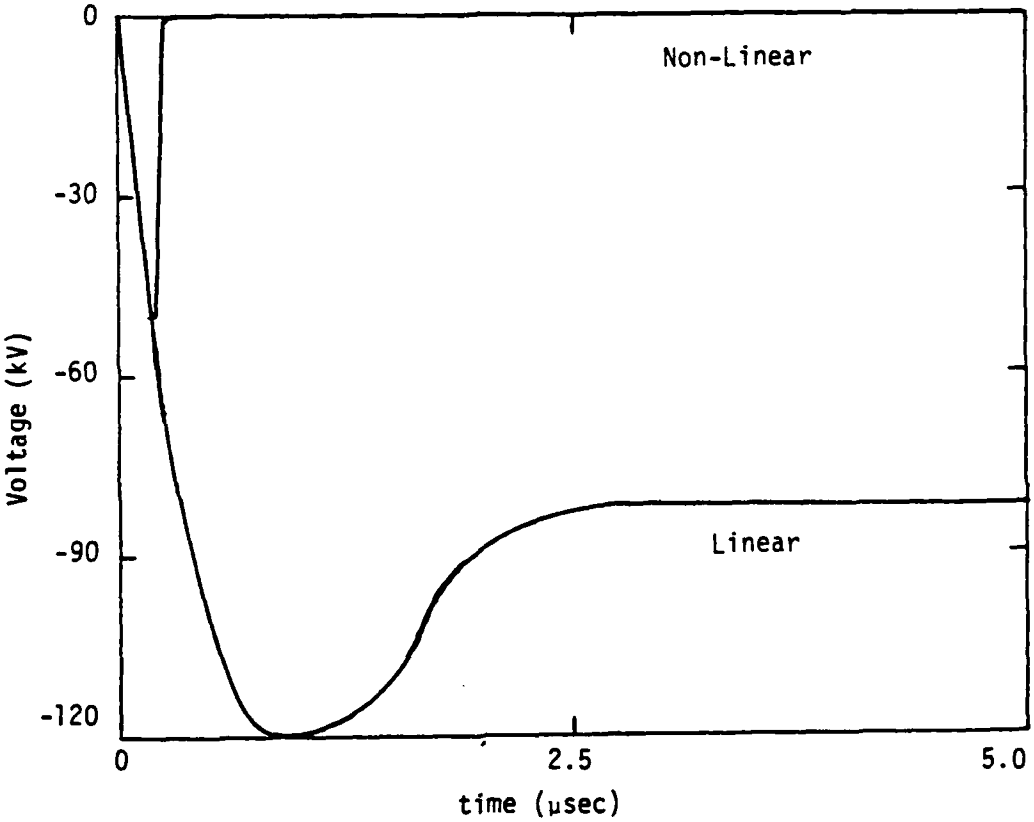

Figure 4.20 Overlay of Linear and Non-Linear Dielectric Voltage at Open End of Cable

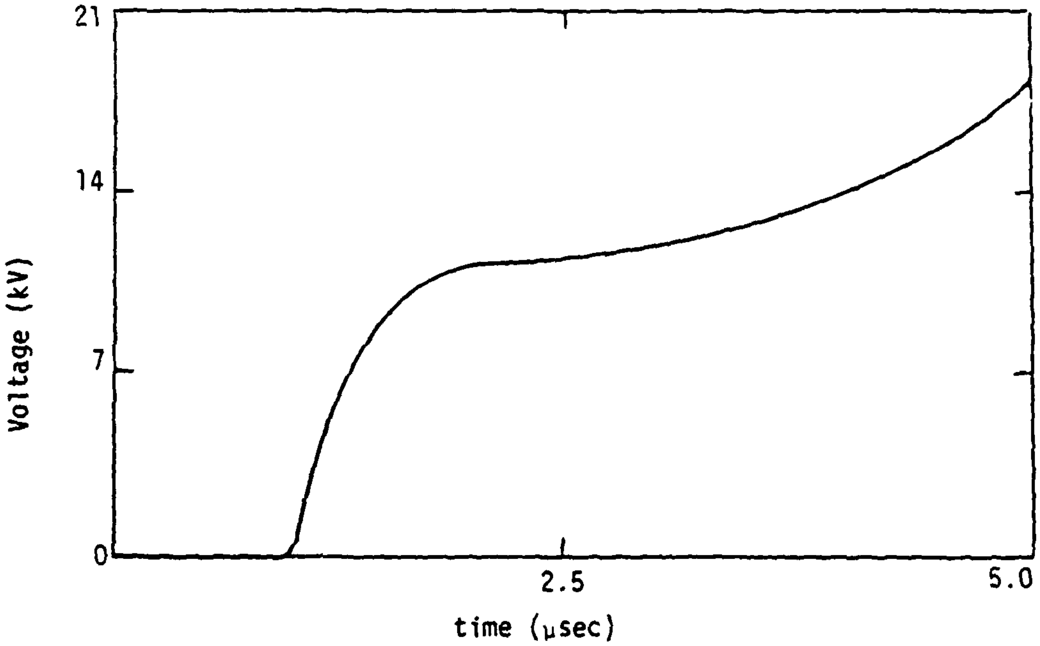

Figure 4.21 Midcable Dielectric Voltage for Linear and Non-Linear Cases

The cable dielectric breaks down only at the open end. The dielectric voltage never again reaches the 50 kV required for breakdown. It is noted that the voltage of Figure 4.21 was calculated out further in time and peaks at 23 kV at 7.5 μsec.

Analysis of the cable response which included the corona model revealed that the corona never really formed. The reason for this is that the impressed air conductivity from the radiation source is so large that it prevents large electric fields from existing in it. These fields were short lived and were only a few hundred kV/m at the most and were thereby not sufficient to cause electron avalanche which is needed to further enhance the conductivity.

4.4 Comparison of Previously Used Environments and Those Used in the Present Study

The response of the surface cable is greatly influenced by the incident electric field and impressed air conductivity. The incident electric field and impressed air conductivity of the previous tactical environment [1] and the tactical environment used in this study are compared. The cable responses are also compared. In this chapter, the term "old" will refer to the electric field and air conductivity used in the previous study and the term "new" will refer to the tactical environment used in the present study.

The radial electric field and air conductivity at 1000 m for the two cases are compared in Figures 4.14 and 4.15. It is seen that the new conductivity is much larger than the old. The new electric field is much larger in amplitude and the energy contained in the pulse is much greater. In fact, if one compares the vales of

$$\int_0^{t_o} E^2 dt \qquad (4.1)$$

for the two environments at 400 meters, one finds that the energy in the new environment is over 5 times greater than the old environment. Although the energy contained in the new pulse is much greater than that in the old pulse, the energy in the new pulse is concentrated at the high frequency end of the spectrum. In the lossy soil and conducting air media, the high frequencies are rapidly attenuated which accounts for the larger cable response in the old environment. The actual cable response depends on the value of

$$\int_0^{t_0} Edt. \tag{4.2}$$

At 400 meters, the integral of the field for the old environment is over 1 1/2 times greater than the new environment. This difference is principally caused by the late time peak in the old field, which is absent in the new field. This means that the cable response to the new field will be less than that caused by the old field, because the cable tends to integrate the field. It should be noted that t_0 is 3.8 μsec. in equations 4.1 and 4.2 which is the latest time value given for the new environment. There is every indication that if the environments were integrated out later in time that the energy in the old pulse would compare closer to the energy in the new pulse and the ratio between the integral of the old and new fields in equation 4.2 would become greater.

Also, because the new air conductivity is so much greater than the old conductivity, the allowed electric field scattered from the wire is correspondingly less, thereby minimizing the possibility of air breakdown from the scattered field.

Short circuit current and open circuit voltage cable responses for these two environments are compared in Figures 4.22 and 4.23. In this case, the cable is identical to that used previously in Section 4.3, except that now the end closest to the source is shorted and the far end is open. These results clearly show the difference in response to the two environments.

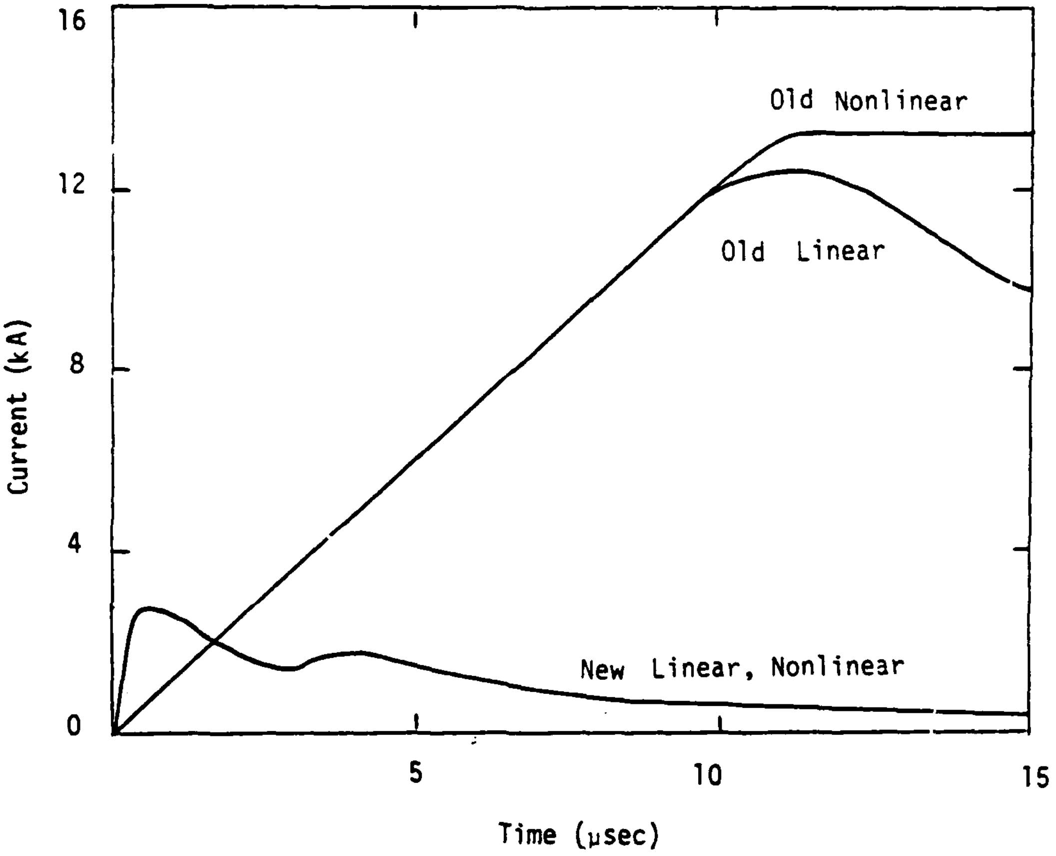

Figure 4.22 Comparison of Short Circuit Current Response from Old and New Environments with a Soil Conductivity of 0.005 mho/m

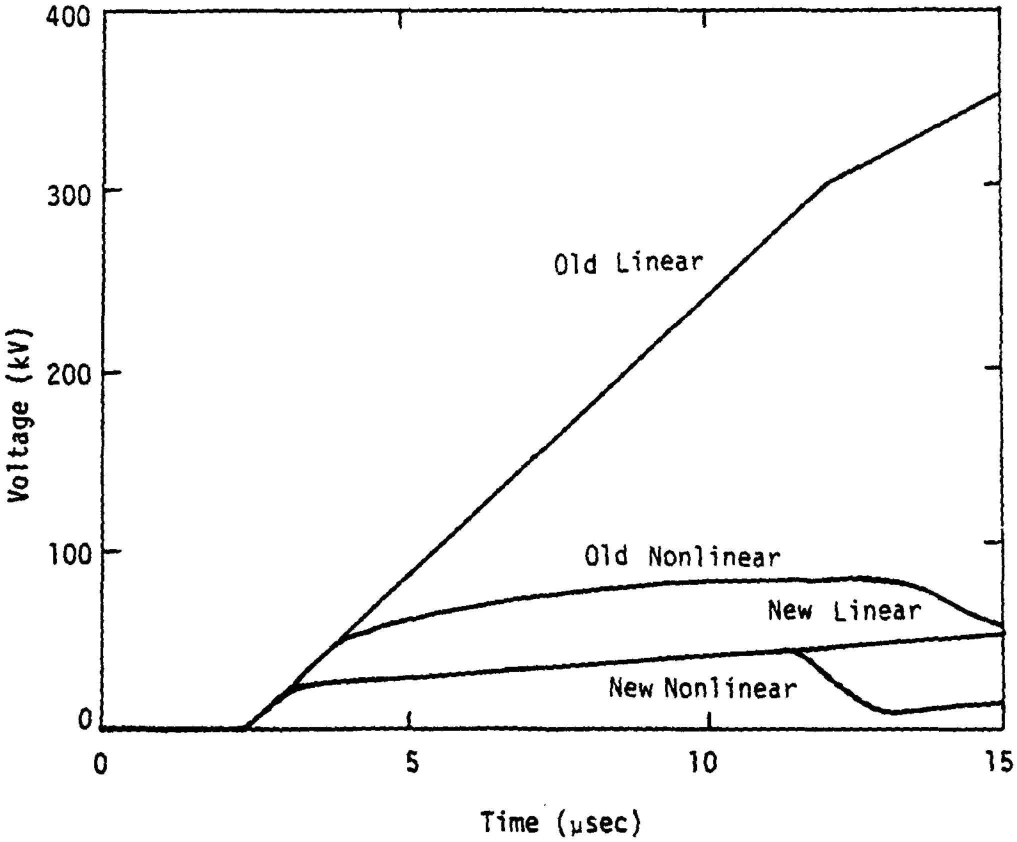

Figure 4.23 Comparison of Dielectric Voltage Response for Old and New Environments with a Soil Conductivity of 0.005 mho/m.

4.5 Angle of Arrival Parameter Study

The angle of arrival affects the cable response. This section examines the response of a 600 m surface cable in the tactical environment at various angles of arrival and variable loads on the far end of the cable. Figure 4.24 shows the location of the nuclear detonation burst point with respect to the surface cable. The far end of the cable is fixed at the range of 1000 m from the burst location and is either short or open circuited. The end of the cable nearest the burst point is open circuited. The end of the cable nearest the burst is rotated an angle α about the fixed end. At $\alpha = 0°$; the cable spans the range 400 to 1000 m(where time = 0 at 400 m). The environment within this range is interpolated. For $\alpha > 70°$, the fixed end of the cable becomes nearer to the burst point than the roving open end. As a consequence, the cable environment is interpolated between the ranges of 600 and 1200 m(where time = 0 at 600 m).

The cable used in the angle of arrival parameter consists of the outer shield and insulating jacket of RG-8. The inner conductor was not considered. The breakdown strength of the dielectric jacket is 1333 V/mil. The earth conductivity is .005 mho/m and the relative permittivity is 10.

In section 4.3, it was found that air breakdown from the scattered fields in the tactical environment is negligible. That is, for the tactical environment, the effects of dielectric breakdown are dominant. Consequently, the angle of incidence parameter study is performed with and without dielectric breakdown.

The results of this study are shown in Figures 4.25 through 4.37. The cable response at the ends and at midcable are presented. In all cases, the cable response is shown in true perspective at each angle for the nonlinear (dielectric breakdown) result unless stated otherwise.

The first angle of arrival parameter studied is for the case where the fixed end of the cable is short circuited to ground. The results of this case are shown in Figures 4.25 through 4.30.

The dielectric broke down for small angles of arrival on the open end of the cable. At $\alpha = 0°$, the dielectric broke down at the two cells nearest the open end at 220 and 967 ns from open to shorted end respectively.

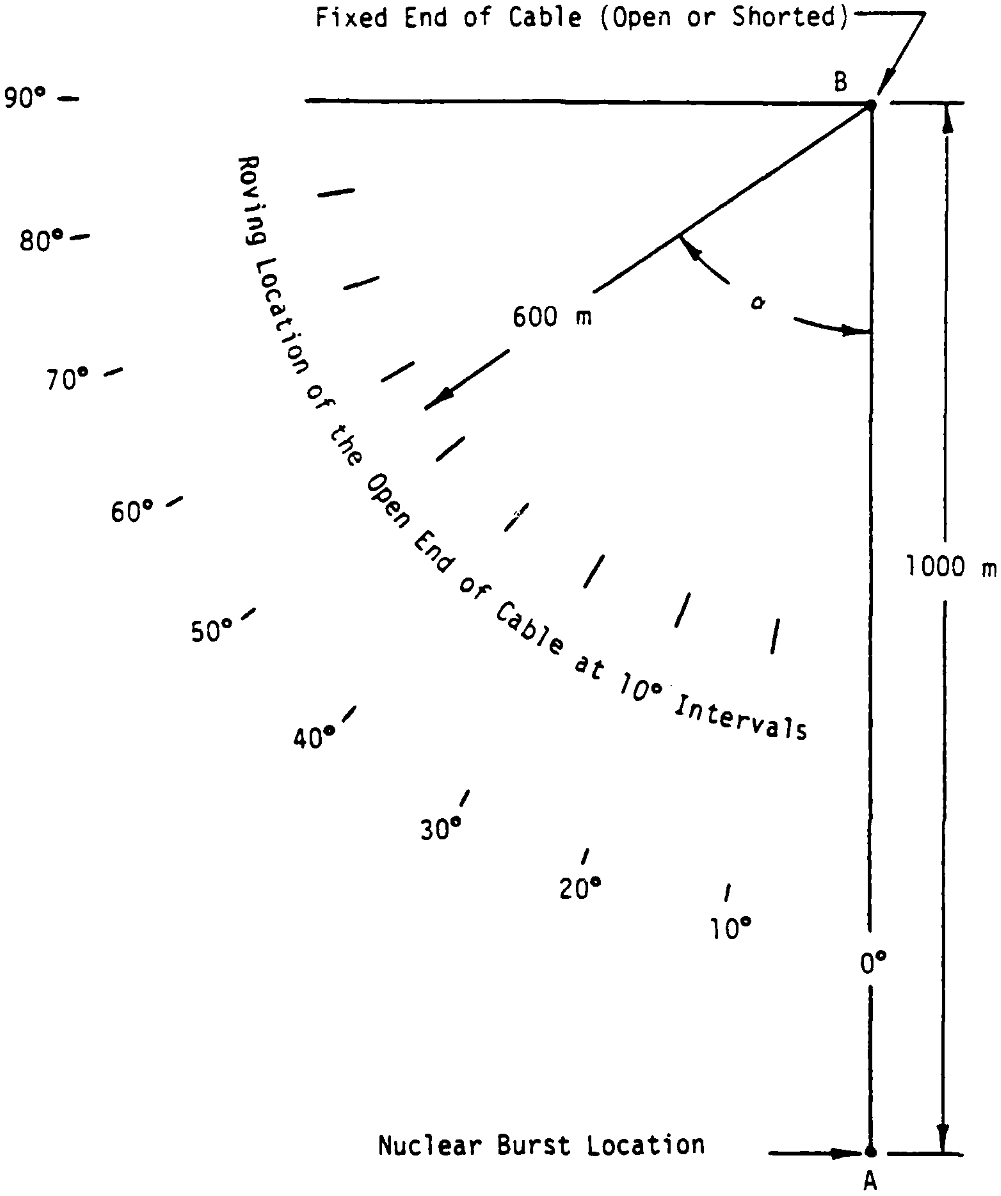

Figure 4.24 Surface Cable Orientation for Angle of Arrival Parameter Study

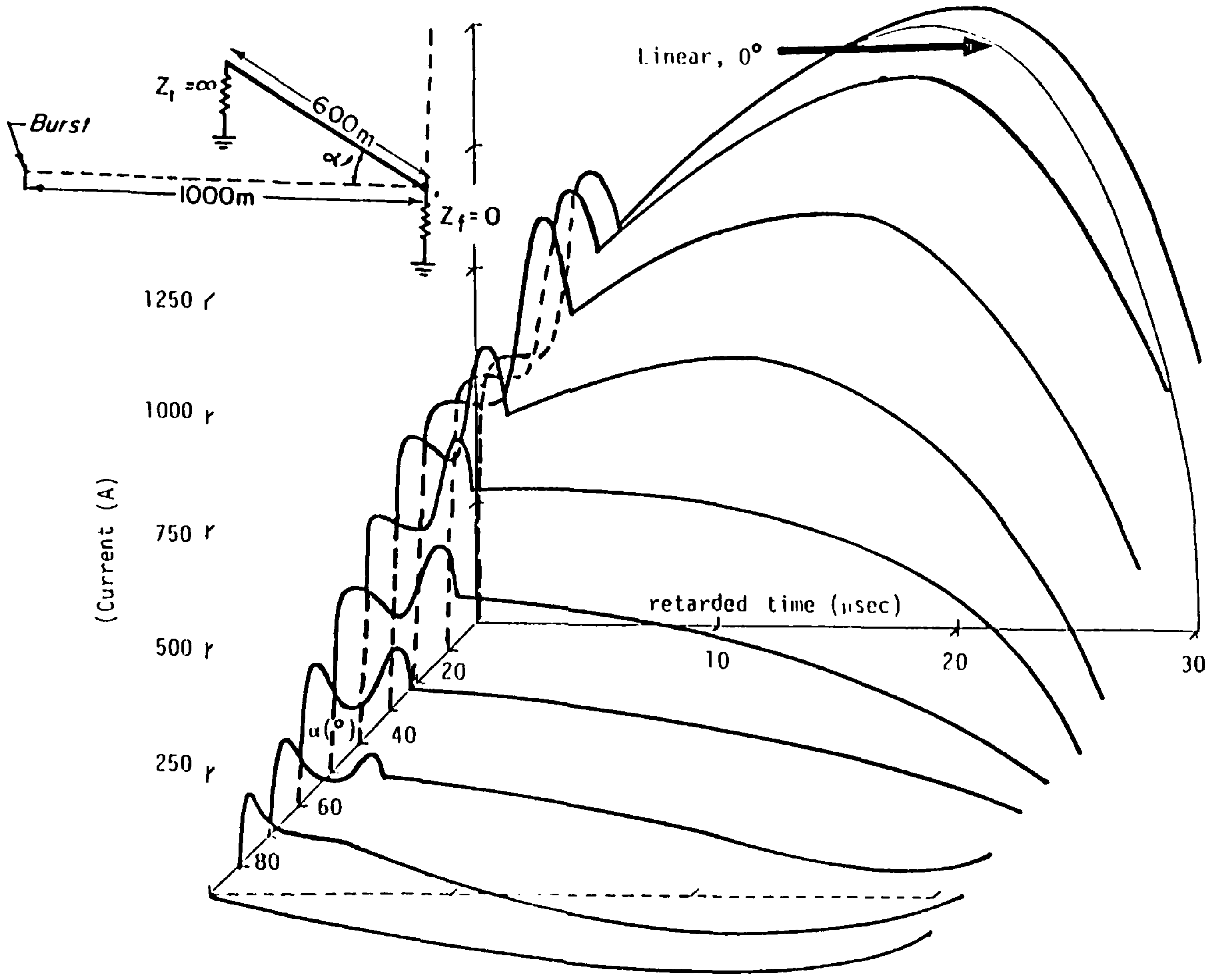

Figure 4.25 Short Circuit Current for Fixed End Shorted

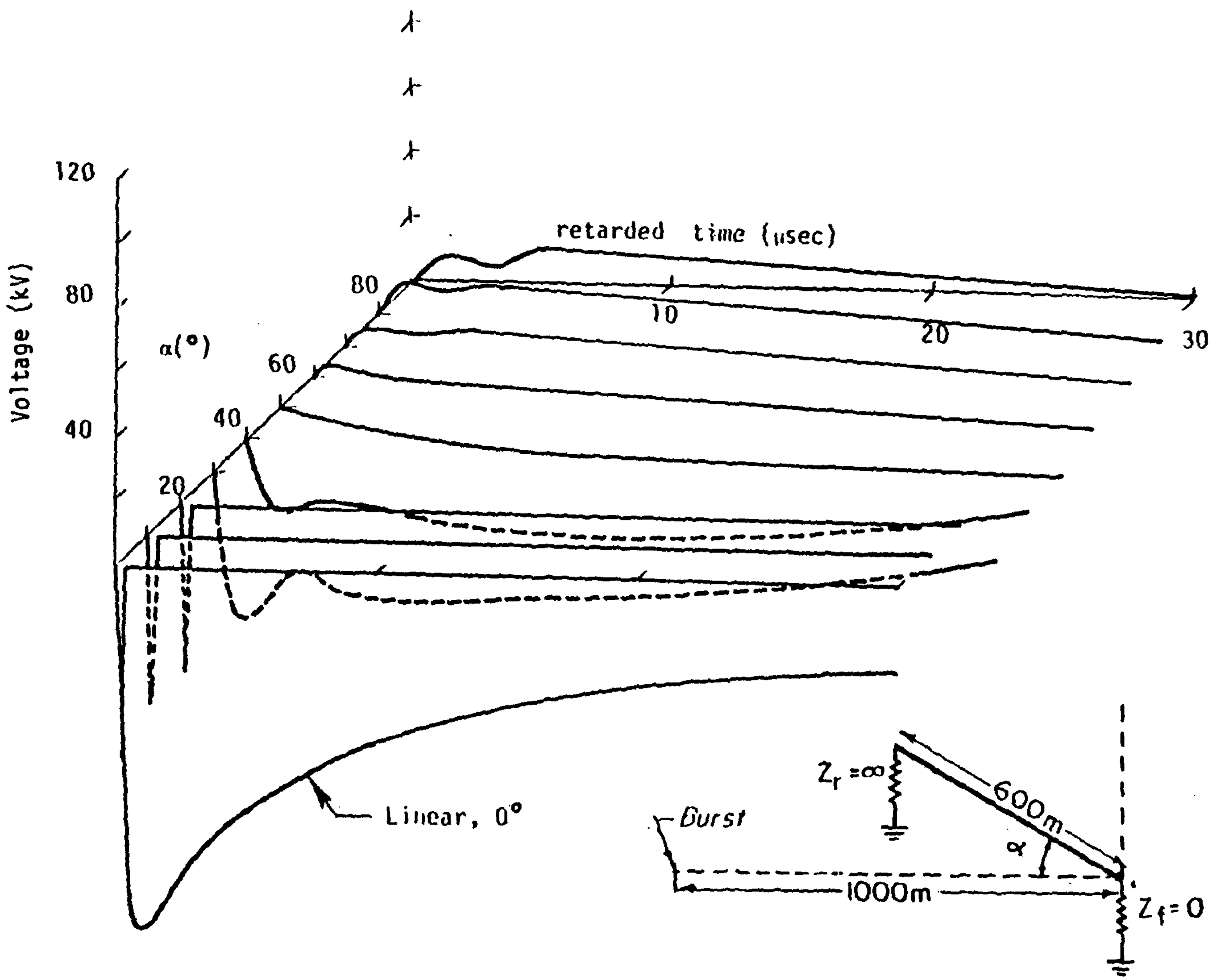

Figure 4.26 Dielectric Voltage on Open End for Fixed End Shorted

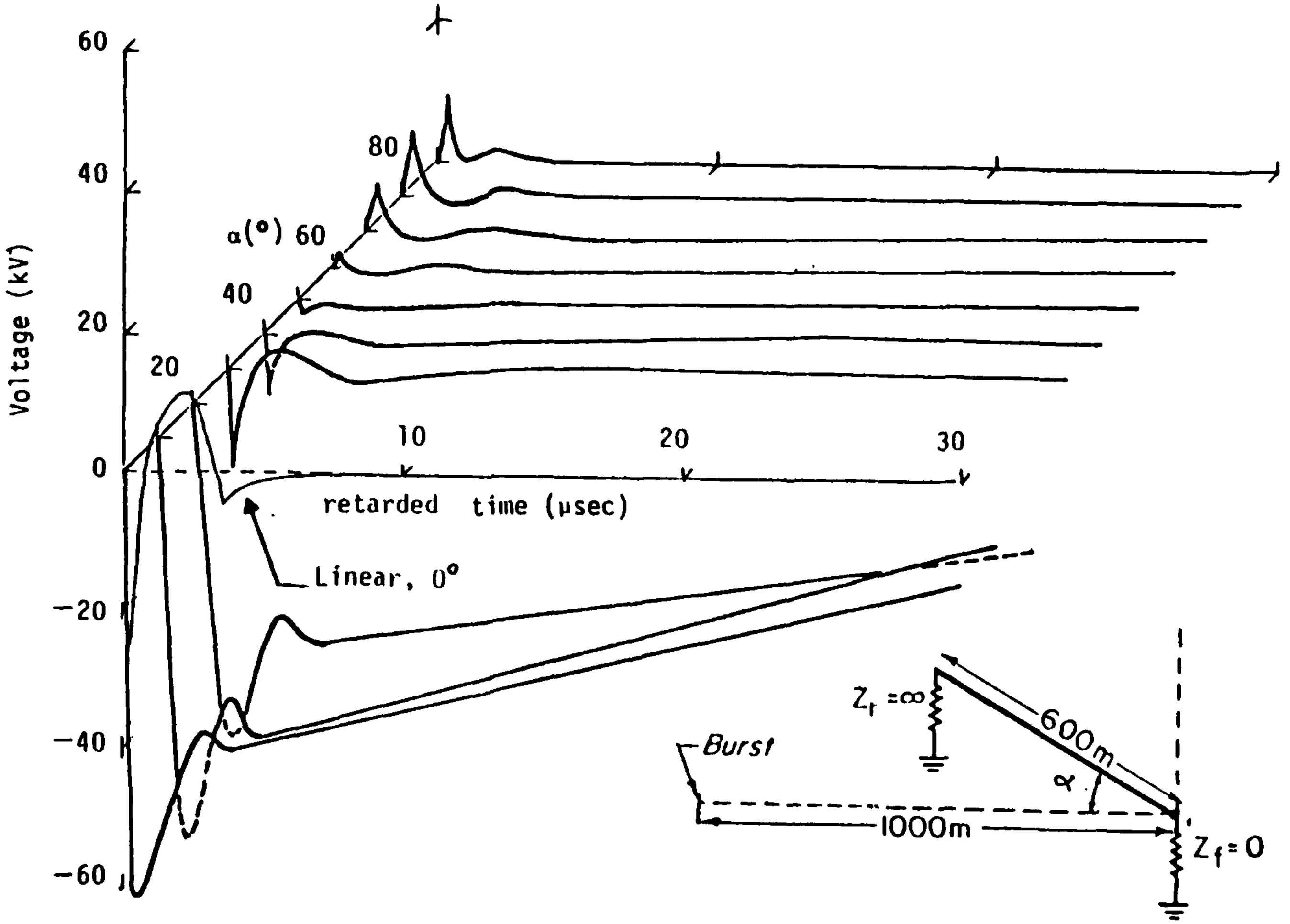

Figure 4.27 Soil Voltage on Open End for Fixed End Shorted

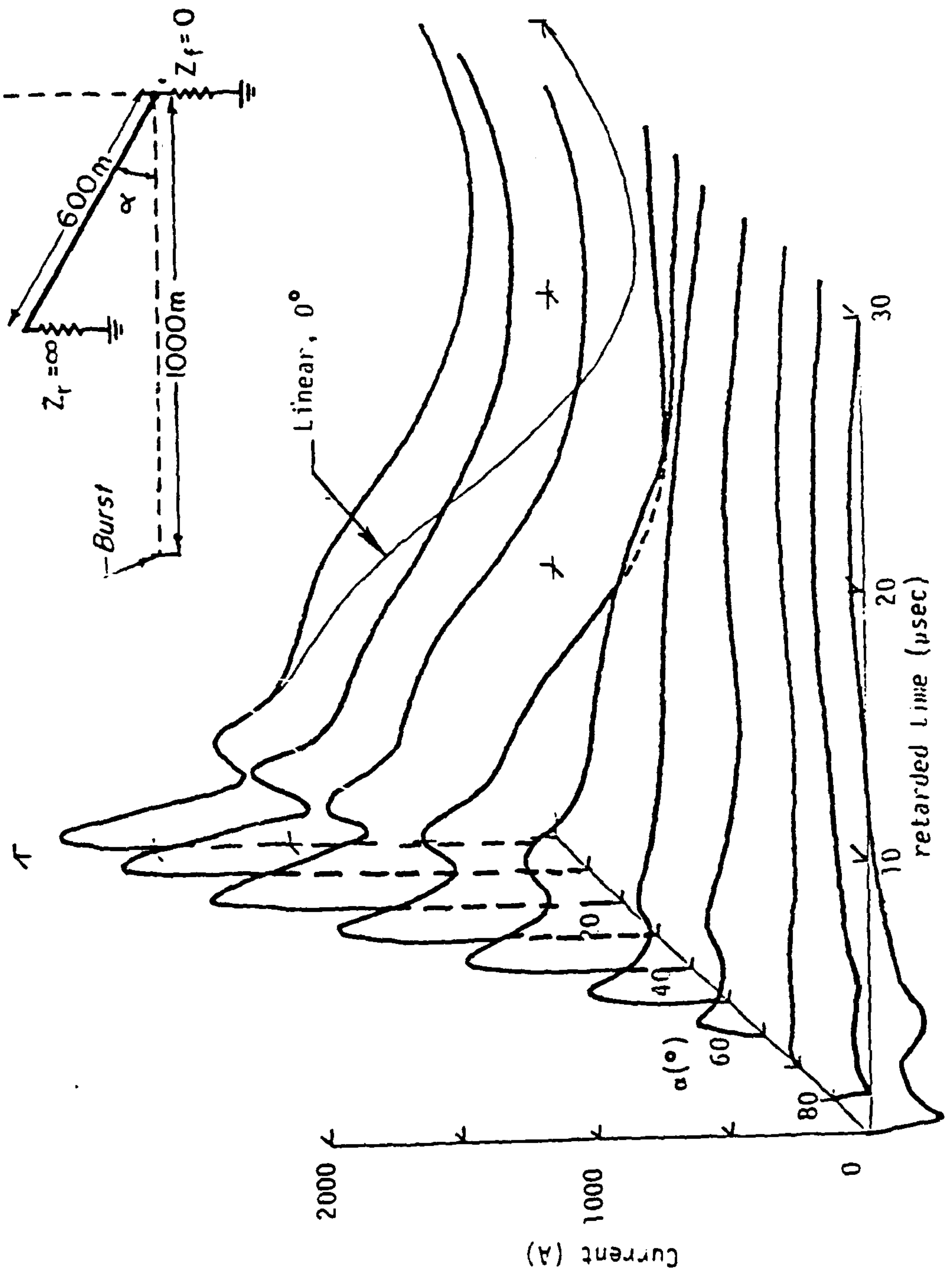

Figure 4.28 Midcable Current for Fixed End Shorted

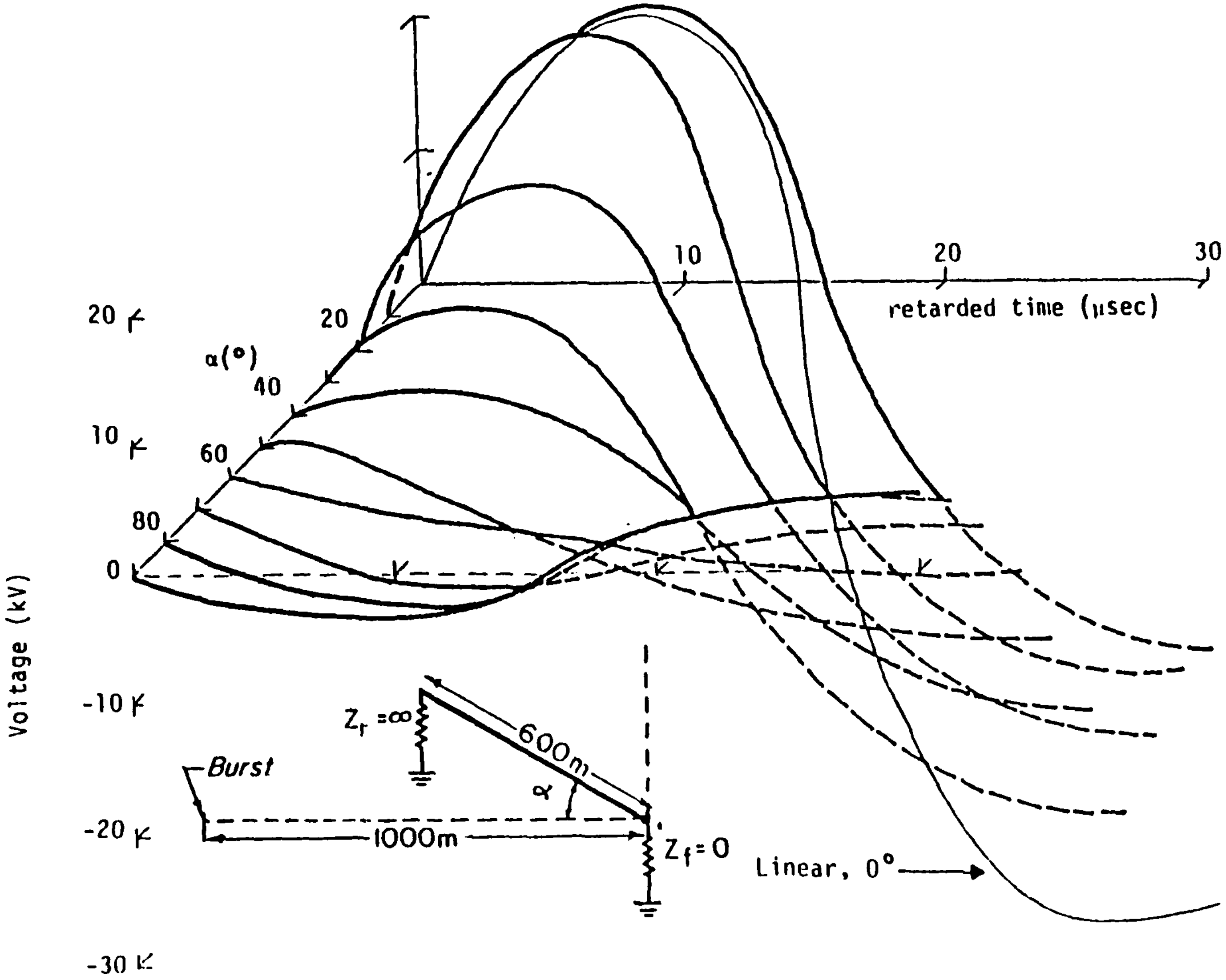

Figure 4.29 Midcable Dielectric Voltage for Fixed End Shorted

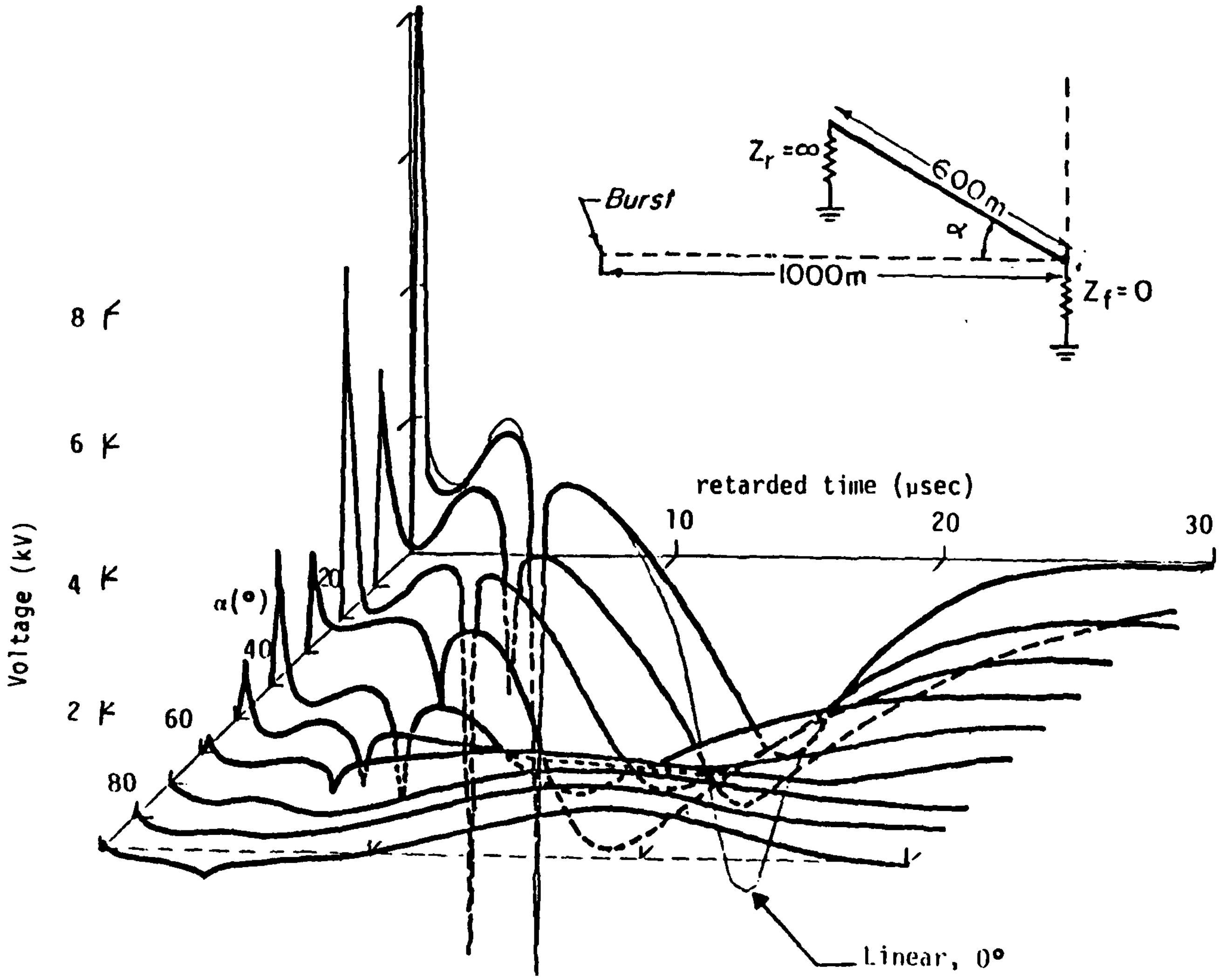

Figure 4.30 Midcable Soil Voltage for Fixed End Shorted

At α = 10°, the dielectric punctured at the two cells nearest the open end at 307 and 1187 ns from open to shorted and respectively. At α = 20°, the dielectric broke down at 580 ns at the open end. For α = 20°, the dielectric broke down at 580 ns at the open end. For α >20°, the dielectric did not puncture.

Figure 4.25 shows the short circuit current for the fixed end of the cable shorted to ground. Comparing the linear and nonlinear result at 0°, there is a 2% increase in the peak current when the dielectric breaks down. The general pulse shape closely follows the incident pulse of Figure 4.14. The saddle shape of the current response occurs when the source reverses polarity. The sharp bend in the pulse shape at 5 μsec occurs due to setting the incident field to zero at that time.

Figure 4.26 depicts the dielectric voltage at the open end of the cable. The dielectric does indeed break down at 0°, 10°, and 20°. Comparison of the linear and nonlinear response at 0° shows a 50% reduction in the peak dielectric voltage. The dielectric breaks down at ~50 kV.

Figure 4.27 shows the soil voltage at the open end of the cable. Comparison of the linear and nonlinear results at 0°, shows that the increase in soil voltage at 0°, 10°, and 20° is caused by the dielectric breakdown. This is explained by the instantaneous flow of charge from the cable conductor through the dielectric jacket to the soil.

Figures 4.28 through 4.30 show the midcable response for the case where the fixed end of the cable is shorted. Figure 4.28 shows the midcable current and Figures 4.29 and 4.30 show the midcable dielectric and soil voltages respectively. In all cases where the linear and nonlinear results are compared, the late time response is altered because of the low impedances offered by the dielectric punctures. One of the most pronounced features appears in the midcable soil voltage response of Figure 4.30. The sharp peak at 6 μsec is caused by the reflection from the ends while the initial sharp pulse is caused by the incident EMP. The change in polarity of the midcable current response of Figure 4.28 occurs for angles greater than 70°.

The second angle of arrival parameter study is for the case where the fixed end of the cable is open circuited. The results of this case are shown in Figures 4.31 through 4.37. The open circuit voltage response for both the soil and dielectric are presented along with midcable responses.

The dielectric broke down for small angles of arrival on both ends of the cable. To differentiate between open ends of the cable, the end of the cable that changes position will be referred to as the roving end and the other end is referred to as the fixed end. At α = 0°, the dielectric first broke down at the two cells nearest the roving end at 220 and 967 nsec from roving end to fixed end respectively. Later at 12 μsec, the cable experienced breakdown at 5 cells spanning the range 32 to 16 meters from the fixed end. This was followed by two more locations breaking down 10 nsec later, then 170 nsec later 60 meters from the fixed end, and then finally at 13 μsec the dielectric broke down at 108 meters from the fixed end. At α = 10°, the cable broke down in a similar fashion. The first breakdown occurred at the two cells near the roving end at 307 nsec and 1.2 μsec. Then breakdown at 4 cells spanning the range 44 to 32 meters from the fixed end occurred at 12.77 μsec. This was followed by a complex ordering of dielectric punctures within a 20 nsec time span. In general, the punctures advanced toward both the fixed and roving ends. The dielectric punctured at the fixed end and the last puncture occurred at 13.4 μsec 92 meters from the fixed end. At α = 20°, the dielectric punctured on the roving end at 580 nsec. The cable did not experience dielectric breakdown for angles greater than 20°.

Figure 4.31 shows the dielectric voltage on the roving end of the cable for the fixed end open circuited. Note that the dielectric broke down at cable orientations of 0°, 10°, and 20° as previously discussed.

Figure 4.32 shows the soil voltage on the roving end of the cable. Comparison of the linear and nonlinear results at 0°, shows that the peak voltage is enchanced 118%. Note the discontinuity of the response between 20 and 30 degrees due to dielectric breakdown.

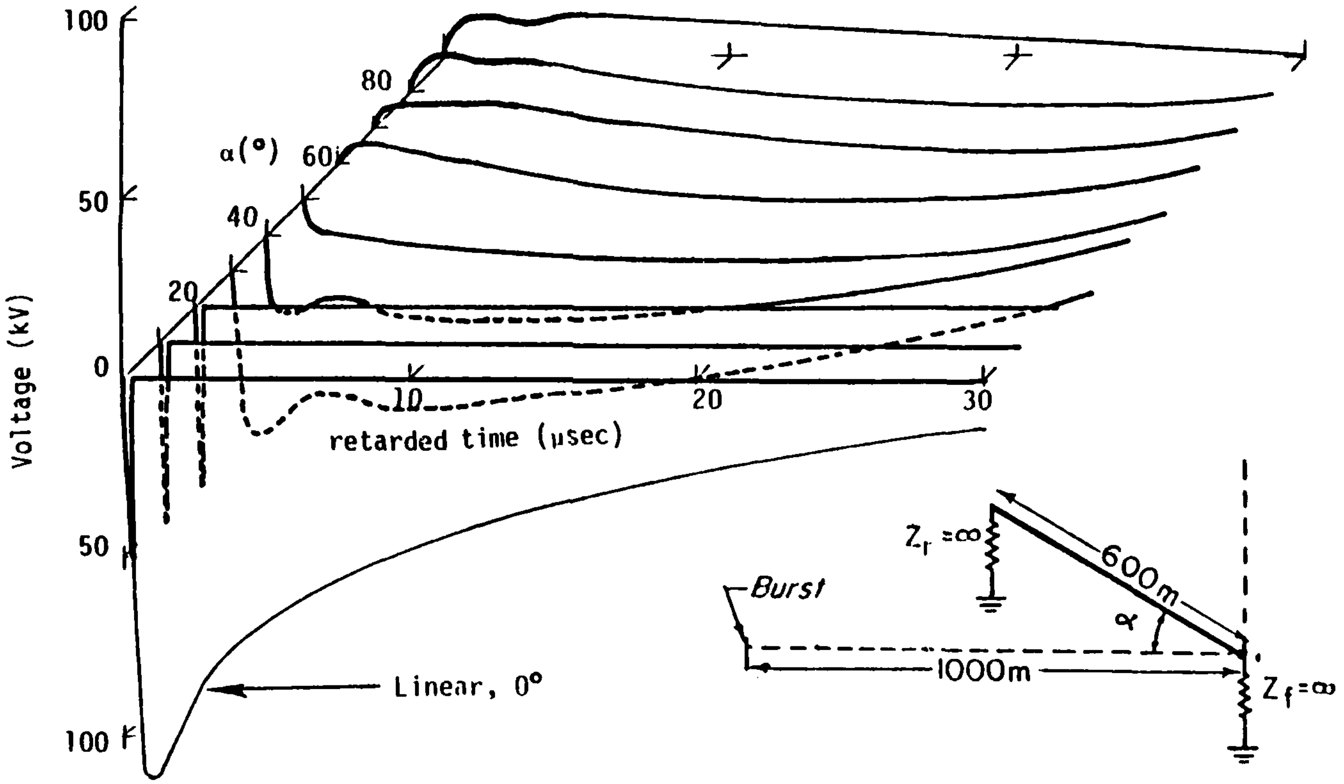

Figure 4.31 Dielectric Voltage on Roving End of Cable for Fixed End Open

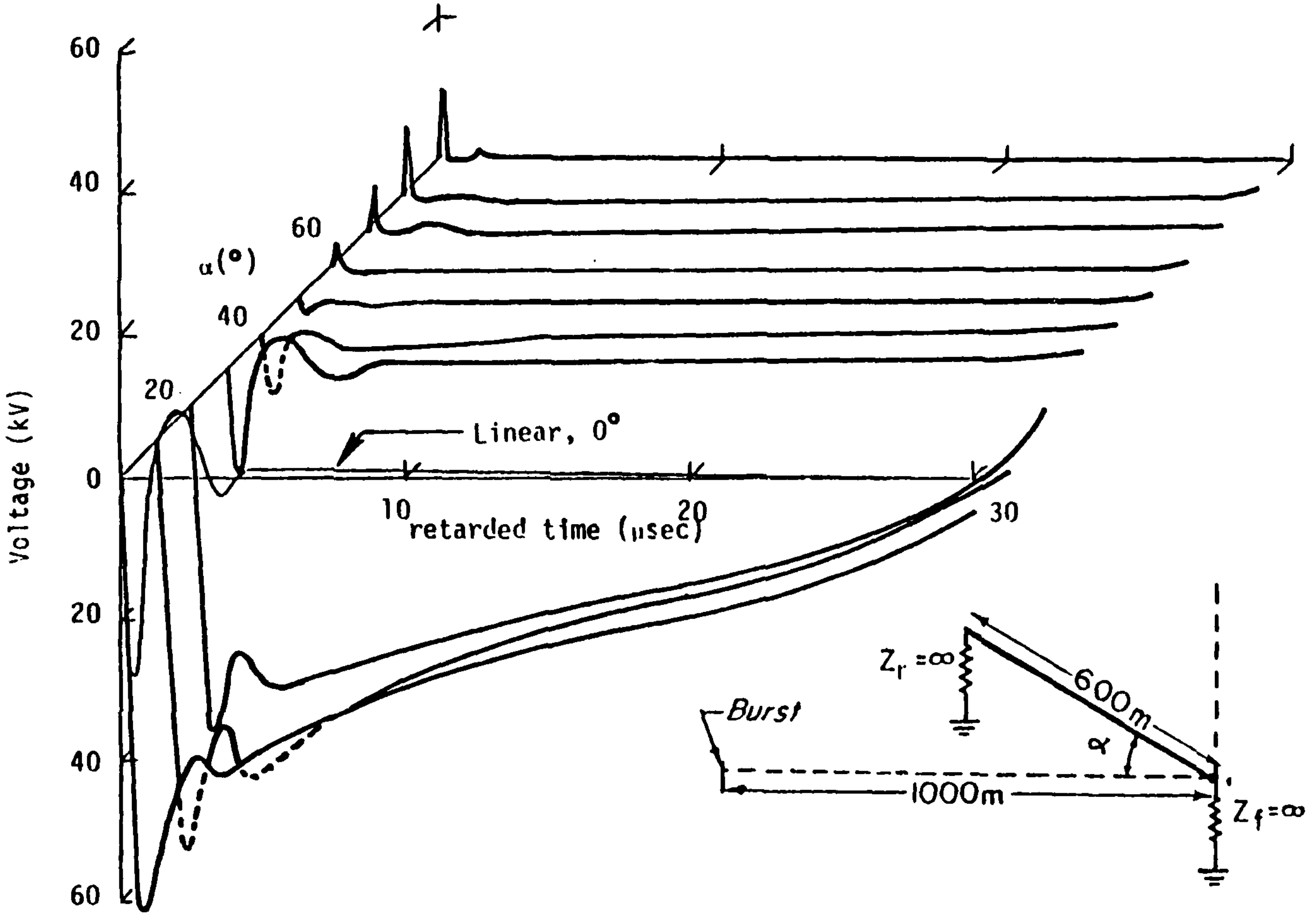

Figure 4.32 Soil Voltage on Roving End of Cable for Fixed End Open

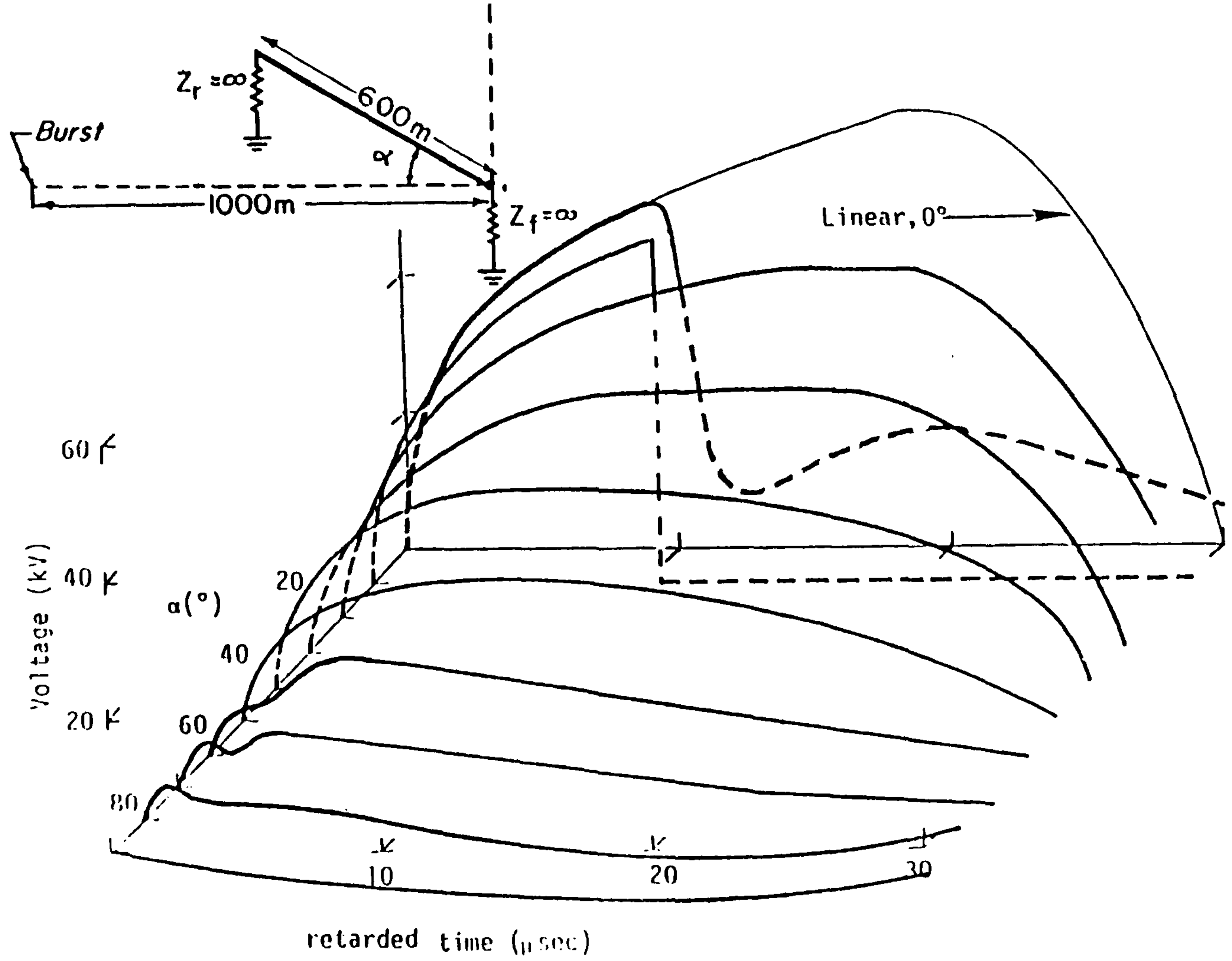

Figure 4.33 Dielectric Voltage on Fixed End of Cable for Fixed End Open

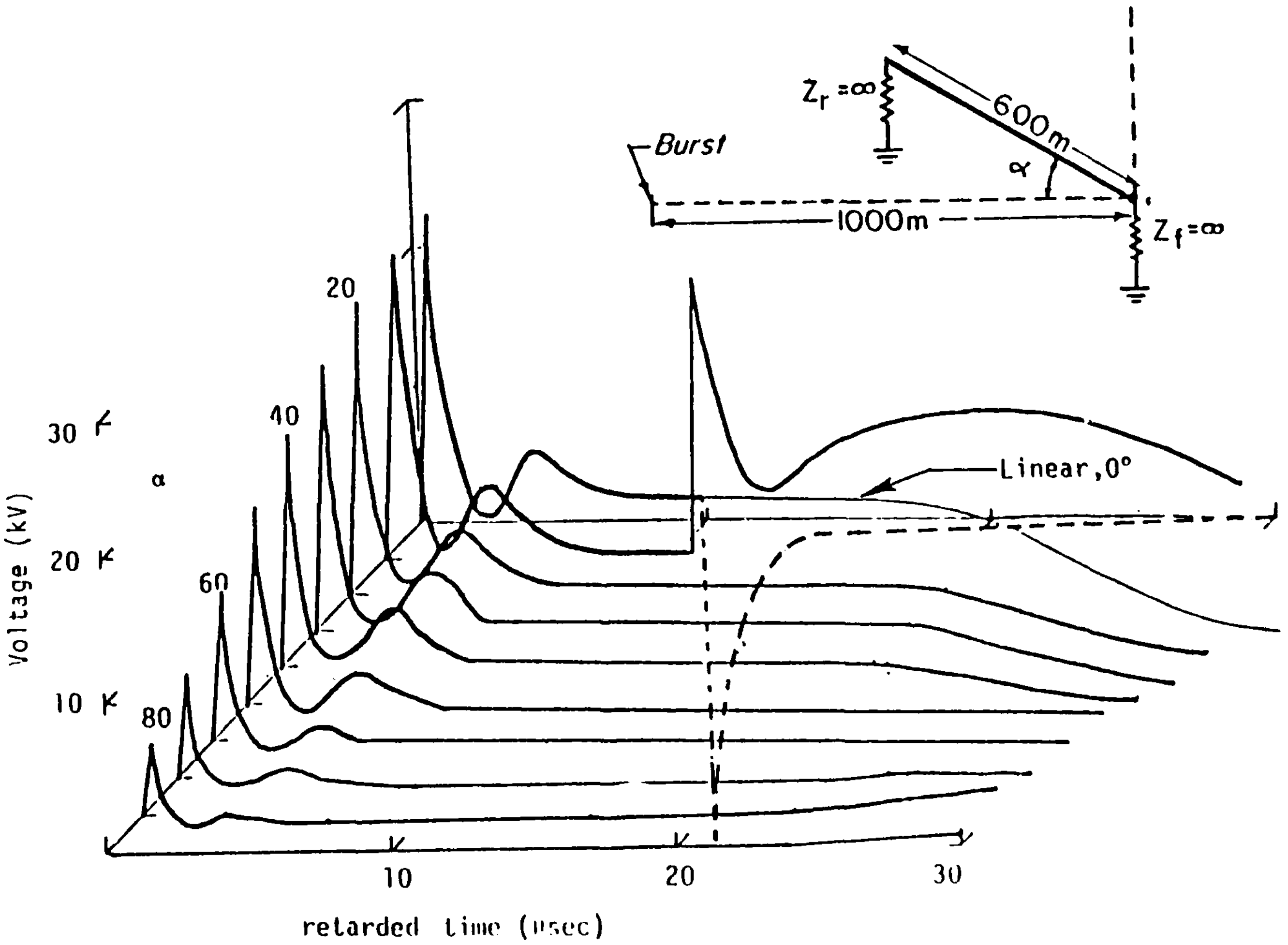

Figure 4.34 Soil Voltage on Fixed End of Cable for Fixed End Open

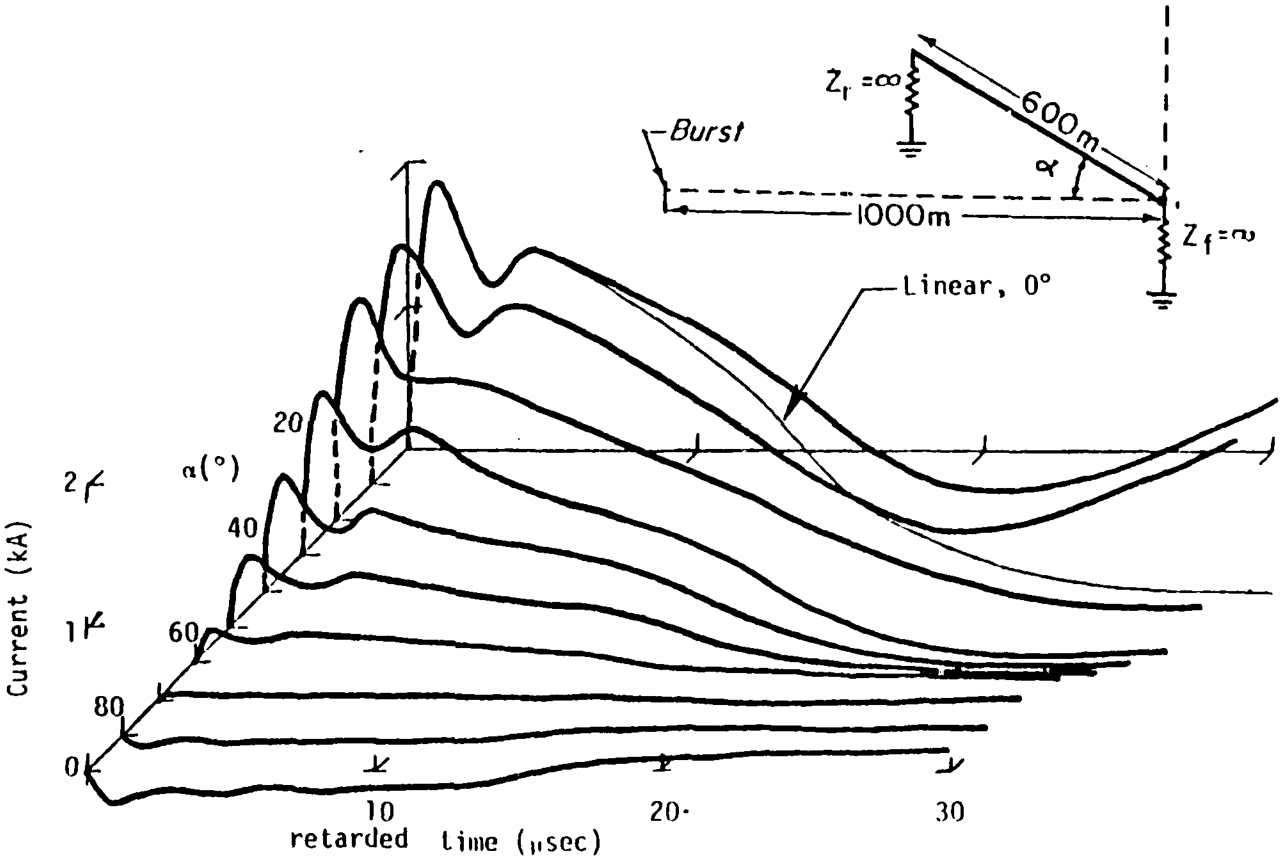

Figure 4.35 Midcable Current for Fixed End Open

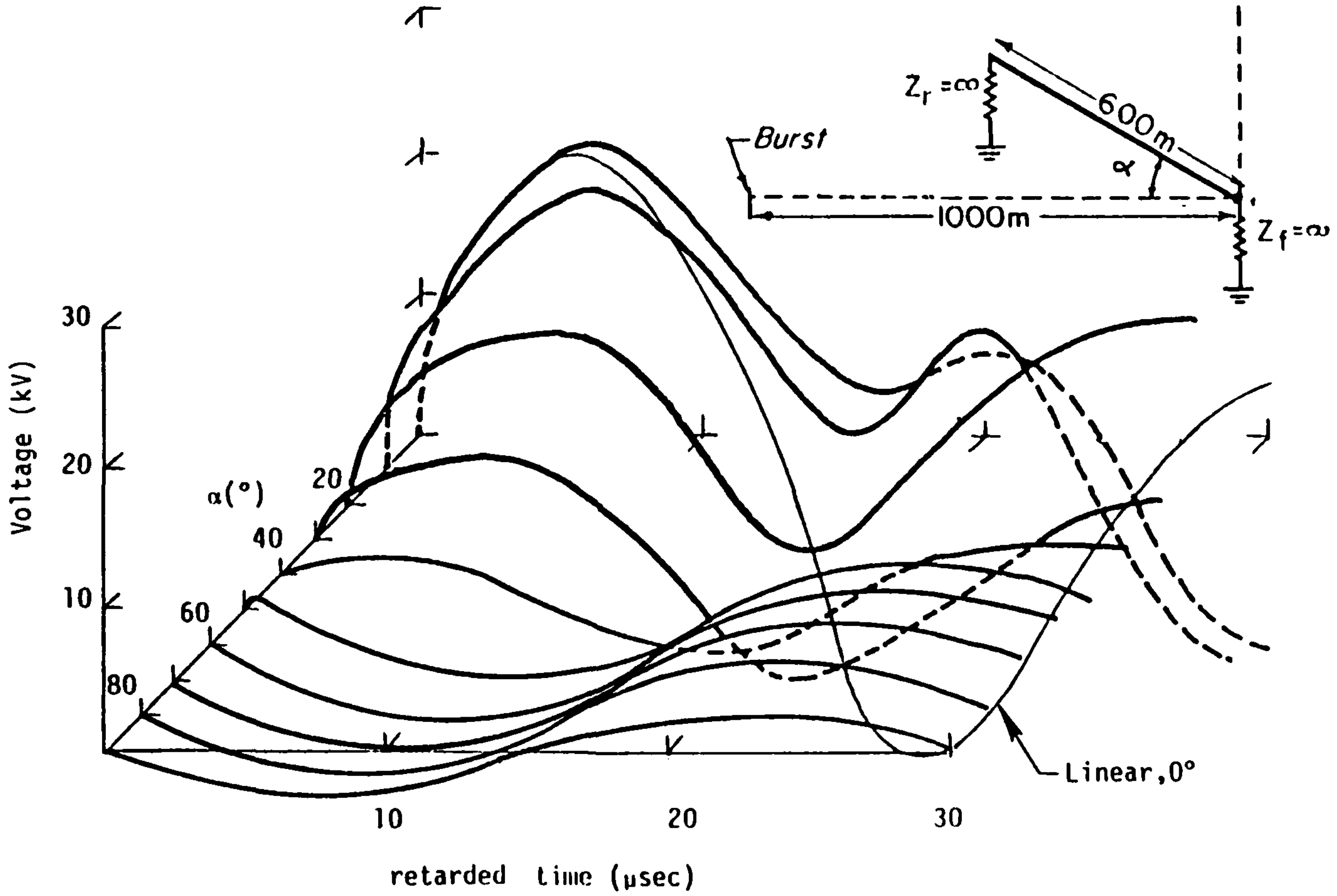

Fiagure 4.36 Midcable Dielectric Voltage for Fixed End Open

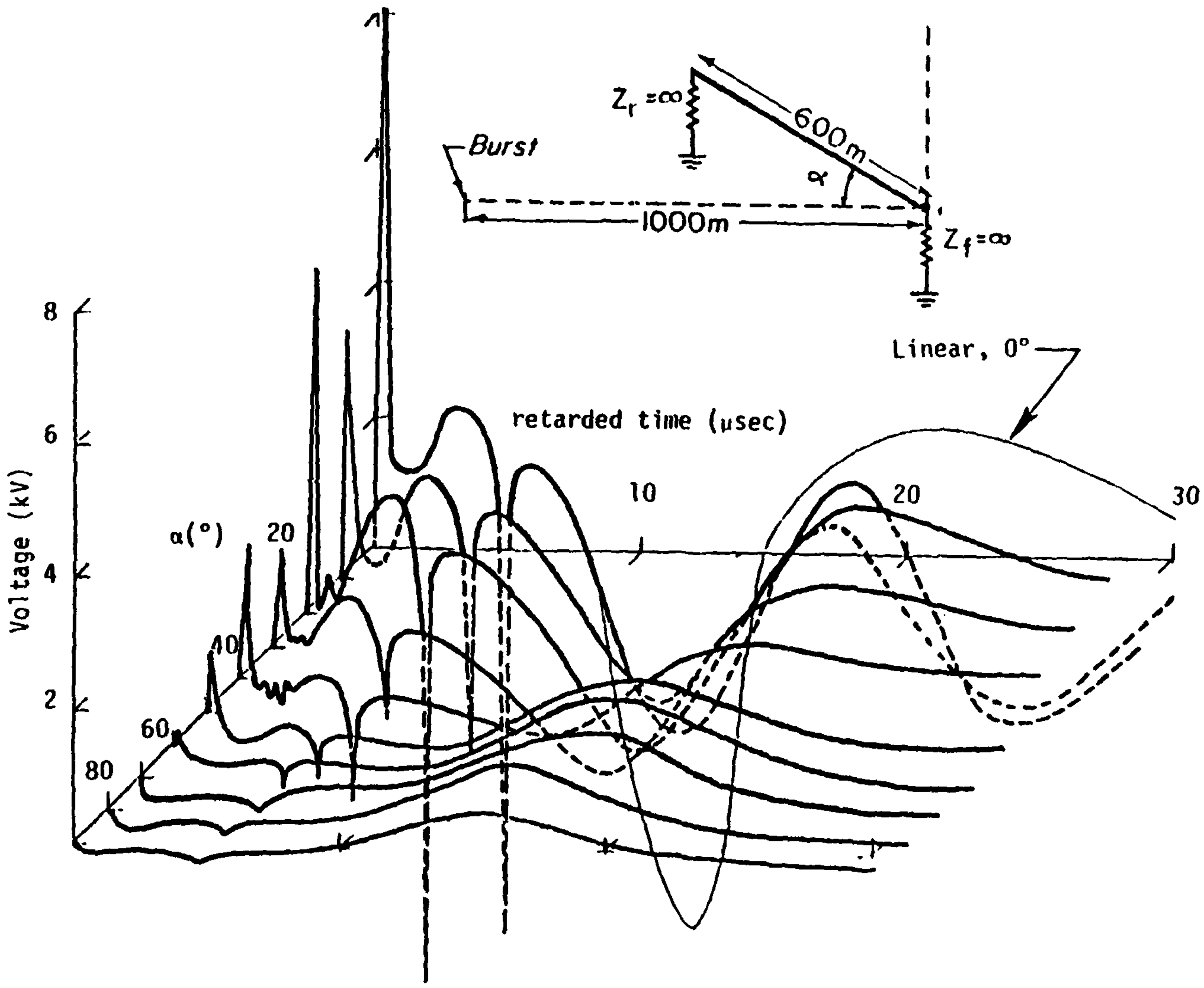

Figure 4.37 Midcable Soil Voltage for Fixed End Open

The dielectric voltage on the fixed end of the cable is shown in Figure 4.33. The voltage response at 10° clearly shows that the dielectric broke down on the fixed end whereas the dielectric broke down near the fixed end at 0° cable orientation. Comparison of the linear and nonlinear results at 0°, shows a 28% reduction in the dielectric voltage caused by puncture.

Figure 4.34 shows the soil voltage on the fixed end of the cable. The change in polarity due to dielectric breakdown at a retarded time of approximately 10 μsec is observed for 0° and 10°. This is explained by the fact that the dielectric did not puncture at the fixed end at 0° but only near the fixed end.

For completeness, the midcable responses are shown in Figures 4.35 through 4.37 for the case where the fixed end is open circuited.

4.6 Computations for the High Altitude Burst (HAB)

Computations for a high altitude burst incident upon a surface cable were made. This study allows evaluation of NEMP surface cable response without the effects of ionizing radiation and impressed air conductivity. The incident field for the HAB predictions was taken to be a plane wave normally incident upon the earth and polarized parallel to the cable. The temporal behavior of the plane wave is the familiar double exponential

$$E_{inc} = 52 \left(e^{-4x10^6 t} - e^{-4.76x10^8 t}\right) \text{ kV/m.} \qquad (4.3)$$

Standard plane wave reflection coefficients were used to obtain the total field at the earth's surface, which is shown in Figure 4.38 for a soil conductivity of 5 mmho/m and a relative soil permittivity of 10. The cable studied was RG-8 100 meters in length which was shorted on one end and open circuited on the other end.

The electric field and corona sheath radius are determined from the dielectric voltage. That is, the electric field inside the dielectric at the radius of the insulating jacket a_2 is

$$E(a_2) = \frac{V_d C_d}{a_2 2\pi\varepsilon_d}, \qquad (4.4)$$

where V_d is the dielectric voltage, and C_d is the capacity per unit length of the insulating jacket. The electric field just outside the insulating jacket is governed by the boundary condition:

$$\varepsilon_d E_{inside} = \varepsilon_o E_{outside} \tag{4.5}$$

where E_{inside} is the electric field inside the dielectric insulating jacket of permittivity ε_d, and $E_{outside}$ is the electric field in the air. The electric field that determines the air conductivity is obtained by extending the field inside the insulating jacket to just outside by the following

$$E(r) = \frac{V_d \varepsilon_d}{\ln\left(\frac{a_2}{a_1}\right) \varepsilon_o r} \tag{4.6}$$

where r is at the middle of the corona sheath (i.e. $(a_{22}+a_2)/2$). Conversely the corona sheath radius is obtained as

$$a_{22} = \frac{V_d \varepsilon_d}{E_{ABR} \ln\left(\frac{a_2}{a_1}\right) \varepsilon_o} \tag{4.7}$$

where E_{ABR} is the breakdown strength of air.

The cable responses to the HAB are shown in Figures 4.39 through 4.41. A comparison with the results of the previous study are shown in each figure. The difference in the linear results in Figures 4.39 and 4.40 are shown to diverge because of the use of time varying transmission line parameters in the present study (i.e., C(t), G(t), L(t), R(t)). For example in this study, $\frac{d}{dt}(CV)$ is used instead of $C(t)\frac{dV(t)}{dt}$ which was used in the previous study. In this study, the dielectric did not break down nor did the soil. This was also demonstrated in the previous study. However, the air did break down. The air first broke down on the open end of the cable at 50nsec and continued to break down roughly every 30nsec at each successive cell toward the shorted end.

Corona can influence the response of a surface cable. Shown in Figure 4.40 is the dielectric voltage on the open end of the cable. A comparison between the linear and nonlinear results show that the dielectric voltage is lowered on the average by 12%. Air breakdown also alters the soil voltage as shown in Figure 4.41. Comparison of the linear and nonlinear results shows the peak soil voltage is raised 9%. The short circuit current, shown in Figure 4.39, is uneffected by corona.

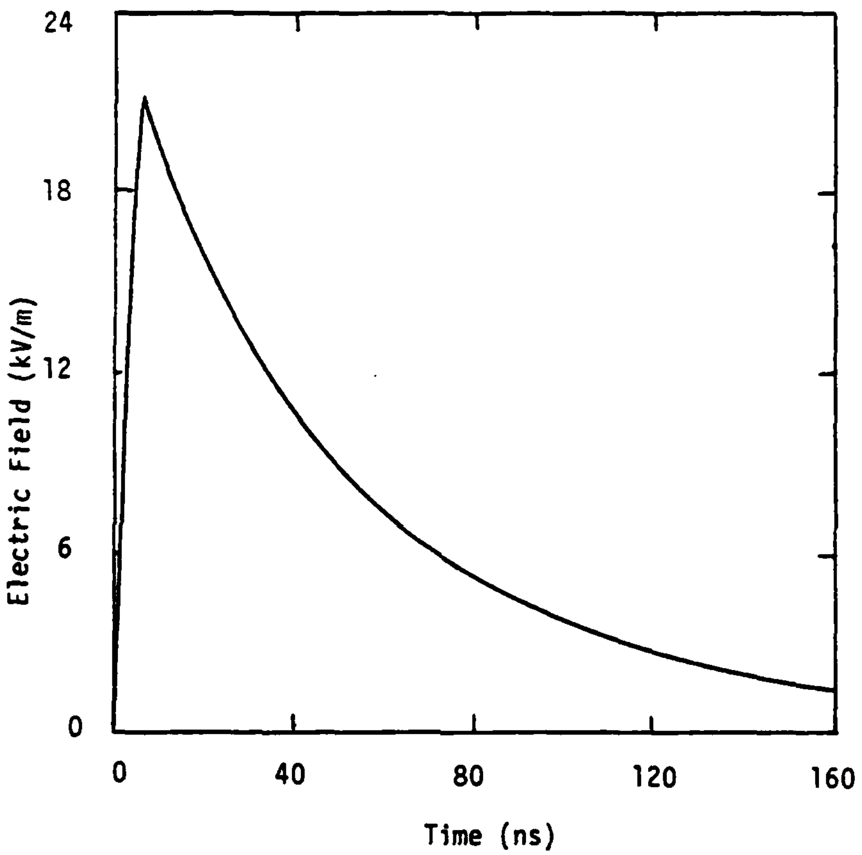

Figure 4.38 Temporal Behavior of HAB at Earth's Surface

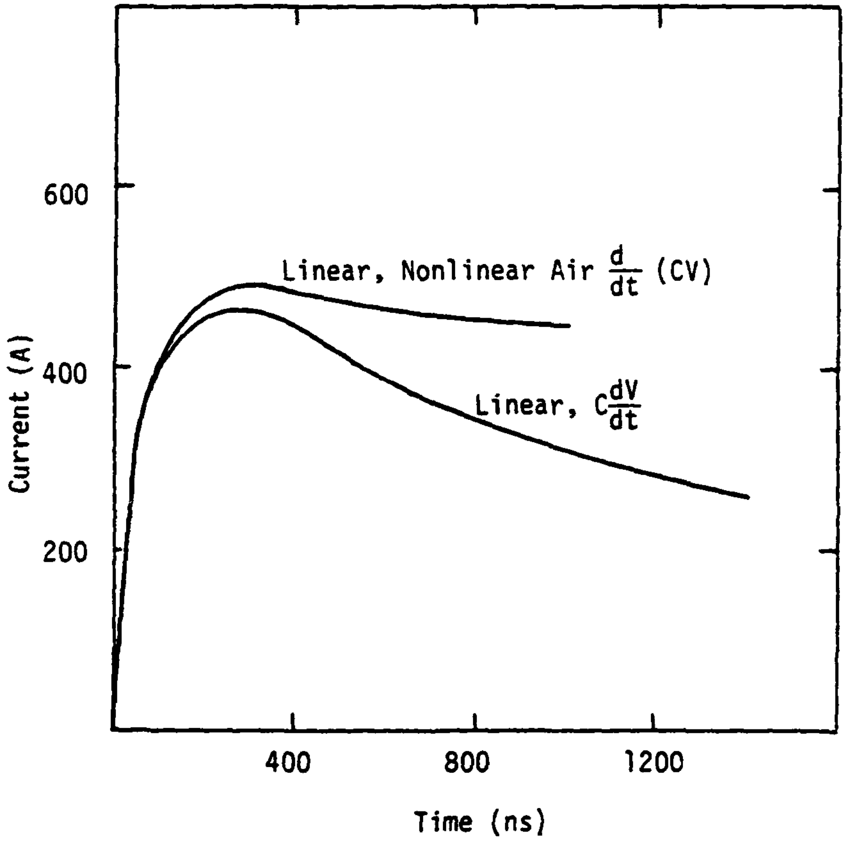

Figure 4.39 Short Circuit Current of Previous (1) Study $[C\frac{dV}{dt}]$ and Present Study $[\frac{d}{dt}(CV)]$

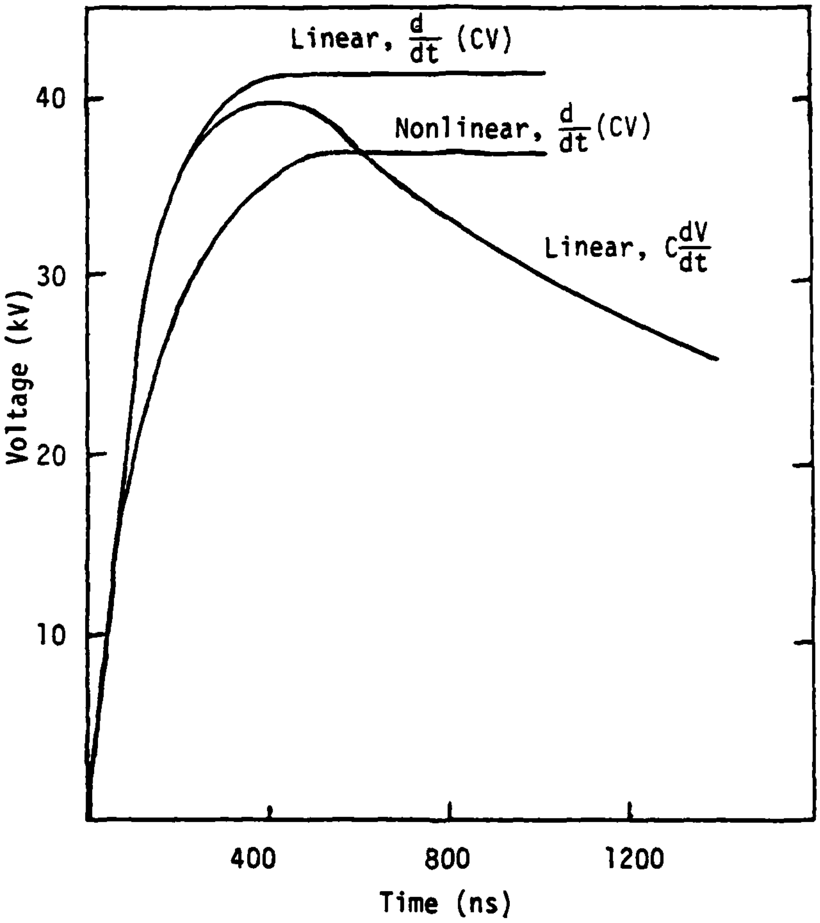

Figure 4.40 Comparison of Open Circuit Voltage Across Dielectric

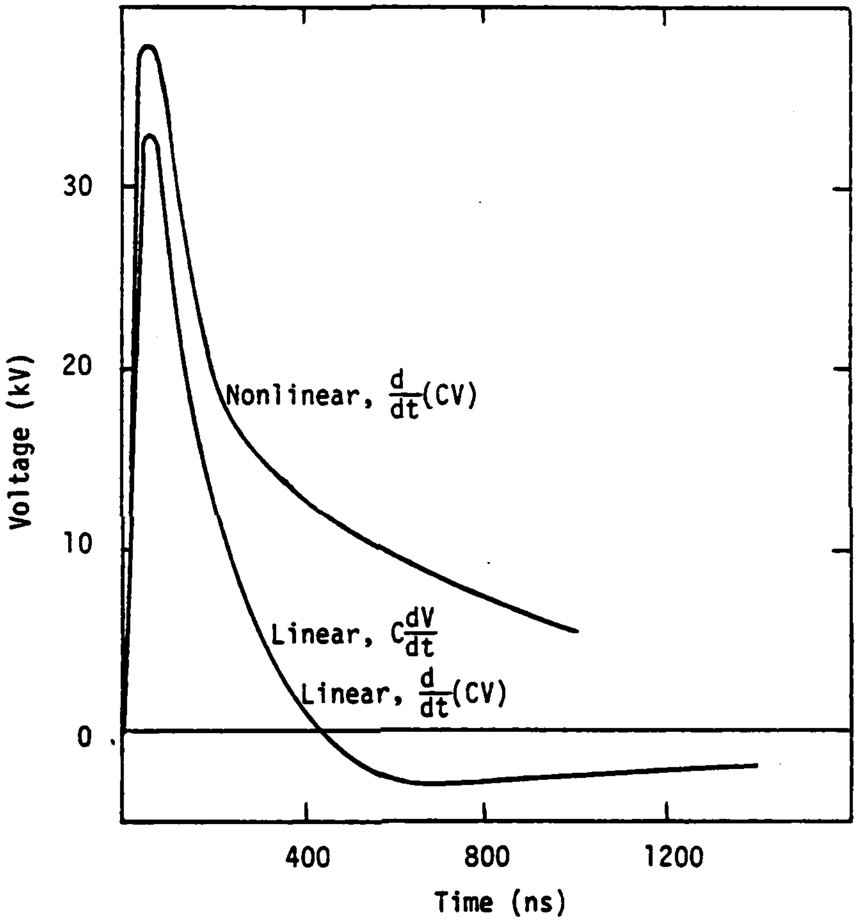

Figure 4.41 Comparison of Open Circuit Voltage Across Soil

CHAPTER 5

SUMMARY AND CONCLUSIONS

In this study, a numerical model for including corona in transmission line analysis was developed. This corona model was then included in a transmission line model which also accounts for nonlinear soil and dielectric breakdown. Corona effects were examined for three cases:

1. An insulated cable elevated in free space above a lossless ground plane.
2. An insulated cable lying on the earth's surface and located in the NEMP source region.
3. An insulated cable lying on the earth's surface and illumined by the high altitude EMP environment.

For a wave normally incident on a cable above a lossless ground plane, the main effect of corona is to increase the current by introducing a narrow current pulse and a corresponding decrease in voltage. For an end on incident wave, the current can be increased by as much as 25%.

It was found that for an insulated surface cable in the source region environment, the impressed air conductivity is large enough that it prevents the buildup of an electric field large enough to cause further air breakdown.

For an insulated surface cable in the HAB environment, corona does occur along the cable, but the effects are apparently diminshed by the lossy cable propagation constant, and no significant effect in the response is noted.

It is emphasized that the air breakdown model used in this study doe not account for arcing or streamering. Except for perhaps cables in the highly conducting source region environments, arcing is likely to happen. The effects of arcing, however, are probably bounded by those caused by dielectric breakdown.

One other observation is worth mentioning. Cable responses were compared for different source region environments. It was found that the largest cable responses are not necessarily caused by the largest peak amplitude incident electric fields. The cable response caused by the high frequency content of the incident fields tends to be highly attenuated by the cable's lossy propagation constant. The cable response is therefore more directly related to the time integral of the low frequency (late time) portions of the incident field. Perhaps a hard look should be taken at the possible source region environments to determine what environment really causes the largest response of surface cables.

REFERENCES

1. Perala, R. A. and Cook, R. B., "The Effects of Dielectric and Soil Nonlinearities on the EMP Response of Cables Lying on the Surface of the Earth," Electro Magnetic Applications, Inc., EMA-79-R-3, January 10, 1979.

2. George A. Farrall, "Vacuum Arcs and Switching," Proceedings of the IEEE, Vol. 61, No. 8, August 1973.

3. Leonard B. Loeb, Electrical Coronas, Their Basic Physical Mechanisms, University of California Press, 1965.

4. John Lam, "Theoretical Study of the Electrical Corona on a Long Wire," Dikewood Corporation, AFWL-TR-76-230, April 1977.

5. William A. Radasky, "An Examination of the Adequacy of the Three Species Air Chemistry Treatment for the Prediction of Surface Burst EMP," DNA 3880T, December 1975.

6. Perala, R. A. and Cook, R. B., "The Effects of Air Breakdown on Antenna Transient Response," Electro Magnetic Applications, Inc., EMA-79-R-1, October 27, 1978.

7. D. E. Merewether, et al, "Electromagnetic Pulse Handbook for Missiles and Aircraft in Flight," Sandia Laboratories SC-M-710346, September 1972.

DISTRIBUTION

ASSISTANT TO THE SECRETARY OF DEFENSE
ATOMIC ENERGY
ATTN MILITARY APPLICATIONS
ATTN EXECUTIVE ASSISTANT
WASHINGTON, DC 20301

DIRECTOR
DEFENSE COMMUNICATIONS AGENCY
ATTN CODE 312
ATTN CODE C313
ATTN CODE 430, PARKER
WASHINGTON, DC 20305

DEFENSE COMMUNICATIONS ENGINEER CENTER
1860 WIEHLE AVE
ATTN CODE R400
ATTN CODE R123, TECH LIB
RESTON, VA 22090

DIRECTOR
DEFENSE INTELLIGENCE AGENCY
ATTN DB 4C2, D. SPOHN
ATTN RTS-2A, TECH LIB
WASHINGTON, DC 20301

DIRECTOR
DEFENSE NUCLEAR AGENCY
ATTN NATA
ATTN TITL (4 COPIES)
ATTN RAEV
ATTN RAEE, G. BAKER (10 COPIES)
ATTN STNA
WASHINGTON, DC 20305

ADMINISTRATOR
DEFENSE TECHNICAL INFORMATION CENTER
ATTN DTIC-DDA (12 COPIES)
CAMERON STATION
ALEXANDRIA, VA 22314

JOINT CHIEFS OF STAFF
ATTN J-3 RM 2D874
WASHINGTON, DC 20301

NATIONAL COMMUNICATIONS SYSTEM
OFFICE OF THE MANAGER
DEPARTMENT OF DEFENSE
ATTN NCS-TS
WASHINGTON, DC 20305

DIRECTOR
NATIONAL SECURITY AGENCY
ATTN TDL
ATTN R-52, O. VAN GUNTEN
ATTN S-232, D. VINCENT
FT GEORGE G. MEADE, MD 20755

COMMANDER
BMD SYSTEMS COMMAND
DEPARTMENT OF THE ARMY
ATTN BMDSC-AOLIB
ATTN BMDSC-HLE, R. WEBB
PO BOX 1500
HUNTSVILLE, AL 35807

DIVISION ENGINEER
US ARMY ENGR. DIV. HUNTSVILLE
ATTN T. BOLT
PO BOX 1600, WEST STATION
HUNTSVILLE, AL 35807

DIRECTOR
US ARMY BALLISTIC RESEARCH LABS
ATTN DRDAR-BLB, W. VAN ANTWERP
ATTN DRDAR-BLE
ABERDEEN PROVING GROUND, MD 21005

COMMANDER
US ARMY COMMUNICATIONS COMMAND
ATTN CC-LOG-LEO
ATTN CC-OPS-WS, CONNELL
ATTN CC-OPS-PD
ATTN CC-OPS-OS
ATTN ATSI-CD-MD
FT HUACHUCA, AZ 85613

CHIEF
US ARMY COMMUNICATIONS SYS AGENCY
DEPARTMENT OF THE ARMY
ATTN CCM-AD-SV
ATTN CCM-RD-T
FT MONMOUTH, NJ 07703

COMMANDER
US ARMY NUCLEAR & CHEMICAL AGENCY
ATTN MONA-WE
ATTN DR. BERBERET
7500 BACKLICK ROAD
BUILDING 2073
SPRINGFIELD, VA 22150

DISTRIBUTION (Cont'd)

COMMANDER
US ARMY TRAINING AND DOCTRINE COMMAND
ATTN ATCD-Z
FT MONROE, VA 23651

BMD CORP
ATTN CORPORATE LIBRARY
7915 JONES BRANCH DRIVE
MCLEAN, VA 22101

BENDIX CORP
COMMUNICATION DIVISION
ATTN DOCUMENT CONTROL
E JOPPA ROAD
BALTIMORE, MD 21204

DIKEWOOD CORPORATION
ATTN TECHNICAL LIBRARY
1613 UNIVERSITY BLVD, NE
ALBUQUERQUE, NM 87102

ELECTRO-MAGNETIC APPLICATIONS, INC.
ATTN D. MEREWETHER
PO BOX 8482
ALBUQUERQUE, NM 87198

GENERAL ELECTRIC CO.
SPACE DIVISION
VALLEY FORGE SPACE CENTER
ATTN J. ANDREWS
PO BOX 8555
PHILADELPHIA, PA 19101

GTE/SYLVANIA
ATTN J. KILLIAN
1 RESEARCH DRIVE
WESTBORO, MA 01581

HONEYWELL, INC.
AEROSPACE & DEFENSE GROUP
ATTN S. GRAFF
ATTN W. STEWART
13350 US HIGHWAY 19 SOUTH
CLEARWATER, FL 33516

IIT RESEARCH INSTITUTE
ELECTROMAG COMPATIBILITY ANAL CTR
ATTN ACOAT
N SEVERN
ANNAPOLIS, MD 21402

IIT RESEARCH INSTITUTE
ATTN I. MINDEL
10 W 35TH ST
CHICAGO, IL 60616

IRT CORP.
ATTN J. KNIGHTON
PO BOX 81087
SAN DIEGO, CA 92138

LUTECH, INC.
ATTN F. TESCHE
PO BOX 1263
BERKELEY, CA 94701

MARTIN MARIETTA CORP
ATTN M. GRIFFITH (2 COPIES)
ATTN J. CASALESE
ATTN B. BROULIK
PO BOX 5837
ORLANDO, FL 32855

MCDONNELL DOUGLAS CORP
ATTN S. SCHNEIDER
ATTN TECHNICAL LIBRARY SERVICES
5301 BOLSA AVE
HUNTINGTON BEACH, CA 92647

MISSION RESEARCH CORPORATION
ATTN J. RAYMOND
ATTN J. CHERVENAK
5434 RUFFIN ROAD
SAN DIEGO, CA 92123

MISSION RESEARCH CORP
ATTN W. CREVIER
ATTN C. LONGMIRE
ATTN EMP GROUP
PO DRAWER 719
SANTA BARBARA, CA 93102

MISSION RESEARCH CORPORATION
ATTN W. STARK
ATTN J. LUBELL
ATTN W. WARE
PO BOX 7816
COLORADO SPRINGS, CO 80933

RICHARD L. MONROE ASSOCIATES
1911 R STREET NW
SUITE 203
WASHINGTON, DC 20009

DISTRIBUTION (Cont'd)

NORTHROP CORP.
ELECTRONIC DIVISION
ATTN LEW SMITH
ATTN RAD EFFECTS GRP
ATTN B. AHLPORT
2301 W 120TH ST
HAWTHORNE, CA 90250

R&D ASSOCIATES
ATTN DOCUMENT CONTROL
ATTN W. GRAHAM
ATTN C. MO
ATTN M. GROVER
PO BOX 9695
MARINA DEL REY, CA 90291

RAYTHEON CO
ATTN G. JOSHI
ATTN H. FLESCHER
HARTWELL ROAD
BEDFORD, MA 01730

ROCKWELL INTERNATIONAL
ATTN B-1 DIV TIC (BAOB)
PO BOX 92098
LOS ANGELES, CA 90009

SEA
MARINER SQUARE
ATTN W. HUTCHINSON
SUITE 127
1900 N. NORTHLAKE WAY
PO BOX 31819
SEATTLE, WA 98103

SRI INTERNATIONAL
ATTN E. VANCE
ATTN A. WHITSON
333 RAVENSWOOD AVE
MENLO PARK, CA 94025

TELEDYNE-BROWN ENGINEERING
ATTN D. GUICE
CUMMINGS RESEARCH PARK
HUNTSVILLE, AL 35807

TRW ELECTRONICS AND DEFENSE SYSTEMS GROUP
ATTN W. GARGARO
ATTN L. MAGNOLIA
ATTN R. PLEBUCH
ATTN C. ADAMS
ATTN H. HOLLOWAY
ATTN E. HORGAN
ATTN J. PENAR
ONE SPACE PARK
REDONDO BEACH, CA 90278

HARRY DIAMOND LABORATORIES
ATTN CO/TD/TSO/DIVISION DIRECTORS
ATTN RECORD COPY, 81200
ATTN HDL LIBRARY, 81100 (3 COPIES)
ATTN HDL LIBRARY, 81100 (WOODBRIDGE)
ATTN TECHNICAL REPORTS BRANCH, 81300
ATTN CHAIRMAN, EDITORIAL COMMITTEE
ATTN LEGAL OFFICE, 97000
ATTN BRANCH 20000
ATTN BRANCH 20240 (10 COPIES)
ATTN BRANCH 21100
ATTN BRANCH 21200
ATTN BRANCH 21300 (10 COPIES)
ATTN BRANCH 21400
ATTN BRANCH 21500
ATTN BRANCH 21000
ATTN BRANCH 22000
ATTN BRANCH 22300 (2 COPIES)
2800 POWDER MILL RD
ADELPHI, MD 20783

END

DATE
FILMED

5 – 83

DTIC